SANISAND-F: Sand constitutive model with evolving fabric anisotropy

International Journal of Solids and Structures 188–189 (2020) 12–31

Contents lists available at ScienceDirect

International Journal of Solids and Structures

journal homepage: www.elsevier.com/locate/ijsolstr

SANISAND-F: Sand constitutive model with evolving fabric anisotropy

Alexandros L. Petalas [a,*], Yannis F. Dafalias [b,c,d], Achilleas G. Papadimitriou [e]

[a] Department of Architecture and Civil Engineering, Chalmers University of Technology, Sweden
[b] Department of Civil and Enviromental Engineering, University of California, Davis, United States
[c] Institute of Thermomechanics, Czech Academy of Sciences, Prague, Czech Republic
[d] School of Applied Mathematical and Physical Sciences, Department of Mechanics, I. Vardoulakis Laboratory of Geomaterials, National Technical University of Athens, Greece
[e] School of Civil Engineering, Department of Geotechnical Engineering, National Technical University of Athens, Zografou 15780, Hellas

ARTICLE INFO

Article history:
Received 28 March 2019
Revised 9 September 2019
Accepted 11 September 2019
Available online 16 September 2019

Keywords:
Constitutive model
Anisotropic critical state theory
Bounding surface
Sands
Fabric

ABSTRACT

In order to incorporate the very important role of evolving fabric anisotropy on the mechanical response of sand, a constitutive model is developed within the frameworks of Bounding Surface plasticity and Anisotropic Critical State Theory in multiaxial stress space. The main new constitutive ingredient is a fabric anisotropy variable A, a scalar measure of the relative orientation between an evolving fabric tensor $\boldsymbol{F}$ and the deviatoric plastic strain rate direction. The variable A affects scalar ingredients of the model quantifying the plastic strain rate, i.e. the plastic modulus and the dilatancy. A comprehensive calibration procedure is fully described and an extensive validation is performed against a very large dataset from 55 monotonic element tests on Toyoura sand provided by various laboratories, loaded under drained and undrained conditions. The introduction of A into the model is the main reason why successful simulation of data is achieved for loading at various orientations of the stress tensor under otherwise same initial conditions of void ratio and confining pressure, and this even if the data often exhibit huge difference of response because of the difference in loading orientation.

1. Introduction

Many researchers have experimentally observed the very significant effect of the anisotropic fabric on stress-strain response of granular soils. Typically such experiments are performed in the hollow-cylinder apparatus (HCA) where the same loading can be applied at different orientation angles α_σ of the axis of the major principal stress σ_1 with respect to the vertical axis z of sample deposition in the cylinder; the orientation is defined in the $r-\theta$ plane, with r denoting the radial and θ the tangential directions in the HCA, shown in Fig. 1. In addition, with $\sigma_1 > \sigma_2 > \sigma_3$, the intermediate principal stress parameter is defined by $b = (\sigma_2 - \sigma_3)/(\sigma_1 - \sigma_3)$, with b equivalent to the Lode angle of the stress tensor. It follows that in the HCA triaxial compression is defined by $\alpha_\sigma = 0^\circ$ and $b = 0$, triaxial extension by $\alpha_\sigma = 90^\circ$ and $b = 1$ while other values of α_σ and b define other modes of shearing.

Miura et al. (1986) performed drained shearing tests on dense Toyoura sand at constant b and a wide range of orientation angles α_σ that remained fixed during shearing, and observed distinctively softer and less dilative response as the angle α_σ increases. This difference becomes more profound in undrained shearing with differently oriented stress principal axes (PA). Yoshimine et al. (1998) reported a large difference in undrained stress paths and corresponding stress-strain curves between the specimens which were sheared firstly under triaxial compression (TC) and extension (TE) with different b values, and secondly sheared with the same b value at different orientation α_σ values. It was observed that in TC the response was dilative while in TE was strongly contractive, leading in some cases to static liquefaction. In shearing under distinct orientations, the larger the α_σ, the softer and more contractive was the behavior, and in cases of large differences in α_σ, the responses differed dramatically, often reaching 1000% difference in deviatoric stress for the same level of deviatoric strain. Such diversity in response under same loading conditions in different orientations in regard to the sample is indisputable evidence of strong fabric anisotropy effects. The concluding remarks of older and recent works in the literature (Vaid and Sivathayalan, 1996; Nakata et al., 1998; Chaudhary and Kuwano, 2003; Sun et al., 2008; Duttine et al., 2009) are consistent; the effect of fabric anisotropy in conjunction with the loading orientation plays a role of cardinal importance in the soil's response.

* Corresponding author.
E-mail addresses: petalas@chalmers.se (A.L. Petalas), jfdafalias@ucdavis.edu (Y.F. Dafalias), apapad@civil.ntua.gr (A.G. Papadimitriou).

https://doi.org/10.1016/j.ijsolstr.2019.09.005
0020-7683/

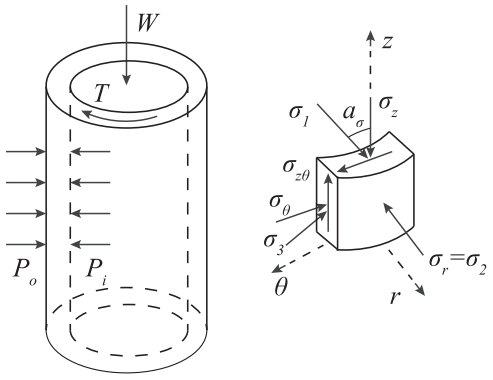

Fig. 1. Element in hollow cylinder specimen and stress components.

Numerical experiments with the use of the discrete element method (DEM) give the opportunity to investigate more thoroughly the mechanics of granular materials and their anisotropic behavior. Using DEM, Li and Li (2009) showed that in transversely isotropic samples, as those created by standard deposition methods in the lab, when α_σ increases and the major principal stress axis deviates from the (gravitational) axis of deposition, the behavior becomes softer and more contractive. They also showed that the void-vector fabric tensor, based on the statistical geometric properties of the void spaces, tends to align at critical state (CS) with the loading direction, identified as the direction of the plastic strain rate tensor. This was also confirmed for the contact-normal and the particle orientation fabric tensors by Fu and Dafalias (2011).

The incorporation of fabric anisotropy in constitutive equations within plasticity theory in an efficient manner is a current research endeavor. Among other approaches, a series of micro-mechanical models have been presented in the literature (Wan and Guo, 2004; Chang and Hicher, 2005; Nicot and Darve, 2007; Wan et al., 2010; Nicot and Darve, 2011), in which the global stress-strain relationship arises by averaging the contact behaviour in the system of grains. This approach avoids some of the phenomenological assumptions of the continuum models, however, its complexity in the formulation and the information that is needed for the grain assembly as input are ongoing research challenges. In this work our focus is on the macro-scale continuum description, while including state variables of the meso-scale like fabric tensors, to describe the anisotropic constitutive behavior of the granular soils.

Within a macroscopic continuum description, Li and Dafalias (2002) and Dafalias et al. (2004) proposed a compatible with Critical State Theory (CST) Roscoe et al. (1958); Schofield and Wroth (1968) modified dilatancy and plastic modulus expressions accounting for the effect of inherent and not evolving fabric anisotropy, by means of a fixed fabric tensor $\boldsymbol{F}$. A corollary of such fixity was that multiple critical state lines (CSL) in the void ratio e - mean effective stress p space were postulated, depending on the way the initial fixed fabric tensor $\boldsymbol{F}$ was related to the loading direction. In order to address this undesirable non uniqueness of CSL and simultaneously account for the effect of fabric anisotropy on dilatancy, Li and Dafalias (2012) introduced the Anisotropic Critical State Theory (ACST), motivated by grain level DEM studies, as a sequel of the aforementioned research works, where the initial fabric tensor evolves towards its critical state value such that a unique CSL in $e-p$ space was obtained. The ACST is not a constitutive model per se, but a framework within which various constitutive models can be constructed. For example, Gao et al. (2014), Gao and Zhao (2017a) and Yang et al. (2018) (only for triaxial loading) proposed models within ACST for monotonic loading and Gao and Zhao (2015a) for cyclic loading, employing the radial mapping rule from a changing projection center within bounding surface plasticity (Mroz et al., 1979; Mroz and Zienkiewicz, 1984; Li, 2002). These models can reproduce the anisotropic behavior of sands under monotonic and cyclic loading, the latter not entirely successfully. However, they suffer from the inherent shortcoming of a radial mapping rule that yields no plastic deformation when neutral loading is applied as the stress point moves tangentially to the loading surface that is necessarily implied by the radial mapping rule.

The main objective of this work is to formulate and apply within ACST, a generalization in the multiaxial stress space of a model shown in Li and Dafalias (2012) for triaxial space only. The operational framework is that of bounding surface (BS) plasticity with kinematic hardening (KH) and a very small size yield surface (YS) along the lines of Manzari and Dafalias (1997) and Dafalias and Manzari (2004) two-surface models. The mapping rule is the classical one associated with two-surface BS plasticity formulations (Dafalias and Popov, 1975; Krieg, 1975; Dafalias and Popov, 1976), which is void of the aforementioned shortcoming associated with the radial mapping rule in BS plasticity. The model belongs to the family of SANISAND models, and because of the role of evolving fabric tensor $\boldsymbol{F}$, it is judiciously named SANISAND-F model. A comprehensive calibration procedure is described, by illustrating step-by-step the analysis of the available experimental data that are used to pinpoint the values of all the model constants. The presented details of this procedure are missing in previous works focusing on the formulation of models within the ACST, in particular those along the SANISAND platform. Additionally, an extensive validation is performed against a very large dataset from 55 element tests on Toyoura sand provided by various laboratories at various times, loaded under drained and undrained conditions. Previously published papers with models within ACST have not presented such an extensive validation. The introduction of fabric anisotropy into the model is mainly the reason why successful simulation of data is achieved for loading at various orientations of the stress tensor under otherwise same initial conditions of void ratio and confining pressure. It is underlined here that the data often exhibited huge difference of response because of different loading orientations.

It is important to emphasize that the generalization from the triaxial space (Li and Dafalias, 2012) to the multiaxial stress space presented in this work for the first time, is not a trivial task. The use of an evolving fabric tensor $\boldsymbol{F}$ and its effect as proposed by ACST, results in evolving asymmetric appearance of bounding and dilatancy surfaces in multiaxial stress space (see Fig. 3), concepts that do not even exist in triaxial space. Moreover, slight reformulation of fabric-related equations adding new model constants was considered necessary for better performance. Furthermore, kinematic hardening did not exist in the triaxial space formulation of Li and Dafalias (2012), while it is a basic constitutive ingredient in the multiaxial space generalization of the present work. And last but not least, the simulations of loading tests under various orientations of the stress tensor require a multiaxial formulation, and the use of a triaxial formulation for such simulations presented in Li and Dafalias (2012) was done under the disclaimer of not being entirely accurate. Therefore, one must re-simulate the tests appearing in Li and Dafalias (2012), as well as many more, by the only correct way, namely using a multiaxial stress constitutive model; this is accomplished in this work for the first time within the SANISAND family of models. Note that recently Petalas et al. (2019) presented an extension of the SANISAND-F model with exclusive purpose to address the sand response under rotation of stress principal axes at fixed stress principal values, that necessitated the addition of constitutive ingredients not included in the model development here. Consequently, a brief outline of the present model appeared necessarily in the foregoing reference, but the exhaustive details of all perspectives (formulation, calibration,

performance) of what constitutes the core base SANISAND-F model are established for the first time in the present work.

In terms of notation the symbol : implies the trace of the product of two second order tensors adjacent to it, i.e. $\boldsymbol{G}:\boldsymbol{H}=tr(\boldsymbol{GH})$. Any tensor $\boldsymbol{H}$ can be written as $\boldsymbol{H}=H\boldsymbol{n}_H$, where the norm $H=\|\boldsymbol{H}\|=\sqrt{\boldsymbol{H}:\boldsymbol{H}}$ and the unit-norm direction $\boldsymbol{n}_H=\boldsymbol{H}/\|\boldsymbol{H}\|$ such that $\boldsymbol{n}_H:\boldsymbol{n}_H=1$. The symbol $\boldsymbol{I}$ is used for the second-order unit tensor. All stresses are effective, and a superposed dot implies the rate.

2. Outline of anisotropic critical state theory

A brief outline of the Anisotropic Critical State Theory (ACST) proposed by Li and Dafalias (2012) is presented in this section. The fabric anisotropy can be characterized by the deviatoric fabric tensor $\boldsymbol{F}$, an internal variable defined as follows

$$\boldsymbol{F}=F\boldsymbol{n}_F;\quad F=\sqrt{\boldsymbol{F}:\boldsymbol{F}};\quad \boldsymbol{n}_F:\boldsymbol{n}_F=1;\quad tr\boldsymbol{n}_F=0 \tag{1}$$

where F= the norm of $\boldsymbol{F}$; and $\boldsymbol{n}_F$= the unit-norm direction tensor of $\boldsymbol{F}$. The fabric tensor $\boldsymbol{F}$ can be in principle associated with the statistical orientation of such entities as particles, contact normal directions or void vectors of a granular assemblage, or a combination thereof.

If $\boldsymbol{R}'$ denotes a tensor along the deviatoric plastic strain rate tensor, the so-called loading direction of ACST is defined by the unit-norm deviatoric tensor $\boldsymbol{n}'=\boldsymbol{R}'/\|\boldsymbol{R}'\|$, where $\|\boldsymbol{R}'\|$ is the norm of $\boldsymbol{R}'$. To characterize the anisotropic sand response, the scalar-valued Fabric Anisotropy Variable (FAV) A was introduced by

$$A=\boldsymbol{F}:\boldsymbol{n}'=F\boldsymbol{n}_F:\boldsymbol{n}'=FN \tag{2}$$

where $N=\boldsymbol{n}_F:\boldsymbol{n}'$ is a scalar measure of relative orientation between $\boldsymbol{n}_F$ and $\boldsymbol{n}'$, as well as a measure of possible difference in eigenvalues even if $\boldsymbol{n}_F$ and $\boldsymbol{n}'$ have the same eigenvectors. Note that in Li and Dafalias (2012) the symbol $\boldsymbol{n}$ is being used instead of $\boldsymbol{n}'$, while here $\boldsymbol{n}$ will be used to represent the normal to the yield surface in the deviatoric stress space.

The fabric tensor is a continuum internal state variable for every model within the ACST. Its rate evolution equation will be presented in more detail in the sequel. Li and Li (2009) and Fu and Dafalias (2011) showed with the use of the Discrete Element Method (DEM) in 2D, that the fabric tensor $\boldsymbol{F}$ evolves with plastic deformation towards a value $\boldsymbol{F}_c$ at CS that has a direction $\boldsymbol{n}_F=\boldsymbol{n}'$ and a norm F_c that depends on the Lode angle θ_F defined by $cos3\theta_F=\sqrt{6}tr\boldsymbol{n}_F^3$. More recently Yang and Wu (2016) confirmed the foregoing by means of 3D DEM; among other things they have shown that the CS norm F_c is independent of the pressure p if it is normalized by the specific volume $1+e$, a normalization shown to be necessary in order to be consistent with thermodynamic dissipation (Li and Dafalias, 2015). Normalizing the norm F by its Lode angle dependent CS value at all states, one has that at CS $F_c=1$ and $\boldsymbol{F}_c=\boldsymbol{n}'$. Consequently, at CS, $N=N_c=\boldsymbol{n}_F:\boldsymbol{n}'=\boldsymbol{n}':\boldsymbol{n}'=1$ and $A=A_c=F_cN_c=1$.

Based on the above, ACST proposes that the two conditions of the classical Critical State Theory (CST) on deviatoric stress ratio and void ratio proposed by Roscoe et al. (1958) and Schofield and Wroth (1968) are enhanced by a third, that refers to the role of fabric, and involves the critical state value of FAV $A=A_c=1$. Thus, according to the ACST, the conditions that are necessary and sufficient to reach and maintain CS are given by

$$\eta=\eta_c=(q/p)_c=M(\theta);\quad e=e_c=\hat{e}_c(p);\quad A=A_c=1 \tag{3}$$

where η= the deviatoric stress ratio and η_c its critical state value; q= the deviatoric stress (equals the square root of the second deviatoric stress invariant); $M(\theta)$= is the Lode angle dependent critical stress ratio, an intrinsic material property; e_c= the value of critical void ratio which is a unique function of p. The third condition $A=A_c=1$ introduced by ACST is not just a convenient and useful supplement of the two first conditions of Eq. (3), but a necessary addition to them, because the two original conditions alone may be necessary but are not sufficient to reach and maintain CS as shown by Theocharis et al. (2017) in 2D and by Theocharis et al. (2019) in 3D loading.

The link between the third CS condition and the elasto-plastic behavior of any model within ACST is the dilatancy state parameter (DSP) ζ, which can be considered to be the modification of the soil's (isotropic) state parameter $\psi=e-e_c$ proposed by Been and Jefferies (1985) in order to include fabric effects. It is given by

$$\zeta=e-e_d=\psi-\hat{e}_A(e,p)(A-1) \tag{4}$$

where $\hat{e}_A(e,p)$= an appropriate positive scalar-valued function of e, p or in the simplest case here, a positive constant. Other possible expressions for ζ are discussed in Li and Dafalias (2012), but Eq. (4) has been found to be very efficient so far. The ζ determines in the $e-p$ space the variable dilatancy state line (DSL) with e_d the void ratio on it at the current p, as shown in Fig. 2b. Based on $\psi=e-e_c$ one has from Eq. (4) that $e_d=e_c+\hat{e}_A(A-1)$, thus e_d can be interpreted as a modified, due to fabric anisotropy, critical state void ratio. Alternatively one can write Eq. (4) as $\zeta=e^\star-e_c$ with $e^\star=e-\hat{e}_A(A-1)$ a modified, due to fabric anisotropy, current void ratio. Notice that at CS where $A=A_c=1$ according to Eq. (3), it follows that $\zeta=\psi=0$ and the DSL becomes identical to the unique CSL in $e-p$ space.

The ζ delineates contractive ($\zeta>0$) and dilative ($\zeta<0$) states under shear within ACST, equivalently to the contractive ($\psi>0$) and dilative ($\psi<0$) states in the classical isotropic CST in terms of ψ. However, notice the important difference that while ψ is independent of the plastic strain rate direction $\boldsymbol{n}'$, the ζ depends on it via A as per Eq. (2); this dependency is visualized in Fig. 2a and 2b when the plastic strain rate direction changes from $\boldsymbol{n}'$ to $-\boldsymbol{n}'$, and consequently A changes to $-A$ that results into a change of ζ as per Eq. (4) and a relocation of the DSL as shown in Fig. 2b; this will have important effects on dilatancy as it will be discussed later in the paper. In the SANISAND-F formulation ζ substitutes for ψ in all the constitutive ingredients, in order to simulate accurately the effect of fabric. The specific propositions for the ζ dependent plastic modulus K_p and dilatancy D are presented in the next sections.

3. The SANISAND-F model

3.1. Basic equations

The effective stress and strain tensors $\boldsymbol{\sigma}$ and $\boldsymbol{\varepsilon}$, respectively, are decomposed into deviatoric and isotropic parts according to $\boldsymbol{\sigma}=\boldsymbol{s}+p\boldsymbol{I}$ and $\boldsymbol{\varepsilon}=\boldsymbol{e}+(1/3)\varepsilon_v\boldsymbol{I}$, where the mean effective stress $p=(1/3)tr\boldsymbol{\sigma}$, the volumetric strain $\varepsilon_v=tr\boldsymbol{\varepsilon}$ and $\boldsymbol{s}$, $\boldsymbol{e}$ are the deviatoric stress and strain tensors, respectively. Note that the all important stress ratio $\boldsymbol{r}$ is defined as $\boldsymbol{r}=\boldsymbol{s}/p$. Assuming the additive decomposition of the total strain rate into elastic and plastic parts, $\dot{\boldsymbol{\varepsilon}}^e$ and $\dot{\boldsymbol{\varepsilon}}^p$, respectively, the rate constitutive equations for a stress or strain rate-driven formulation are given along the lines presented in Dafalias and Manzari (2004) by

$$\dot{\boldsymbol{\varepsilon}}=\dot{\boldsymbol{\varepsilon}}^e+\dot{\boldsymbol{\varepsilon}}^p=\frac{1}{2G}\dot{\boldsymbol{s}}+\frac{1}{3K}\dot{p}\boldsymbol{I}+\langle L\rangle\left(\boldsymbol{R}'+\frac{1}{3}D\boldsymbol{I}\right) \tag{5}$$

$$\dot{\boldsymbol{\sigma}}=2G\dot{\boldsymbol{e}}+K\dot{\epsilon}_v\boldsymbol{I}-\langle L\rangle\left(2G\boldsymbol{R}'+KD\boldsymbol{I}\right) \tag{6}$$

$$\begin{aligned}L&=\tfrac{1}{K_p}\boldsymbol{n}:p\dot{\boldsymbol{r}}=\tfrac{1}{K_p}\boldsymbol{n}:\left(\dot{\boldsymbol{\sigma}}-\tfrac{\dot{p}}{p}\boldsymbol{\sigma}\right)=\tfrac{1}{K_p}\boldsymbol{n}:(\dot{\boldsymbol{s}}-\dot{p}\boldsymbol{r})\\&=\frac{2G\boldsymbol{n}:\dot{\boldsymbol{e}}-K(\boldsymbol{n}:\boldsymbol{r})\dot{\epsilon}_v}{K_p+2G-KD(\boldsymbol{n}:\boldsymbol{r})}\end{aligned} \tag{7}$$

The definition of the loading direction $\boldsymbol{n}$, deviatoric plastic strain rate direction $\boldsymbol{R}'$, dilatancy D and plastic modulus K_p are

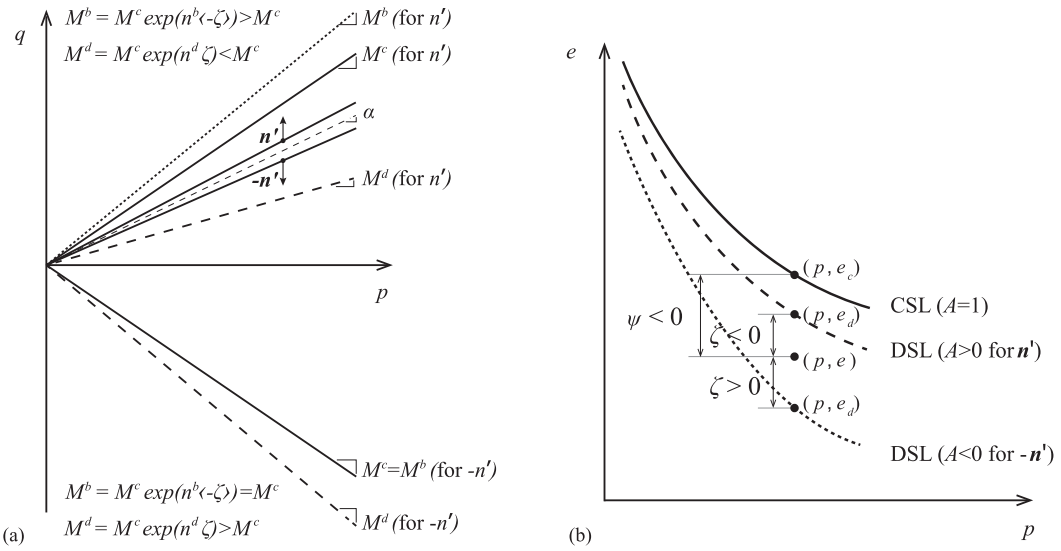

Fig. 2. (a) Schematic presentation of the yield surface, bounding, dilatancy and critical state lines, as well as their dependence on ζ Eq. (12) and the plastic strain rate direction $\boldsymbol{n}'$; (b) illustration of ψ, ζ, CSL and DSL, as well as their dependence on the direction of $\boldsymbol{n}'$.

given in the sequel. The L is the plastic multiplier or loading index, determining plastic loading/elastic unloading according to its sign, hence it is enclosed in Macaulay brackets $< >$.

3.2. Critical state line and elastic moduli

The analytical expression for the unique CSL in the $e-p$ space is given in Li and Wang (1998) as

$$e_c = \hat{e}_c(p) = e_{ref} - \lambda_c (p/p_{at})^{\xi} \tag{8}$$

where e_{ref}, λ_c and ξ = material constants; and p_{at} = the atmospheric pressure.

The hypoelastic formulation proposed by Richart et al. (1970) defines the shear G and bulk K moduli by

$$G = G_0 p_{at} \frac{(2.97-e)^2}{1+e} \left(\frac{p}{p_{at}}\right)^{1/2}; \quad K = \frac{2(1+\nu)}{3(1-2\nu)} G \tag{9}$$

where G_0 = a dimensionless material constant; ν = the Poisson's ratio, while the atmospheric pressure p_{at} is used for normalization. In passing notice, that the hypoelastic law of Eq. (9) neglects fabric anisotropy effects on elasticity for simplicity, especially since the focus of the proposed model is on the large strain response that is mainly plastic while anisotropic elasticity affects mostly the small strain response (Zhao and Gao, 2015).

3.3. Yield surface

The analytical expression of the YS is given by

$$f = [(\boldsymbol{s} - p\boldsymbol{\alpha}) : (\boldsymbol{s} - p\boldsymbol{\alpha})]^{1/2} - \sqrt{\frac{2}{3}} pm = 0 \tag{10}$$

in terms of the deviatoric stress $\boldsymbol{s}$, mean effective stress p and a deviatoric back-stress ratio tensor $\boldsymbol{\alpha}$. It can be visualized as a circular "cone" in $\boldsymbol{s}$, p space with its axis along $p\boldsymbol{\alpha}$ and radius $\sqrt{2/3}pm$. If Eq. (10) is divided by p, the YS is expressed in terms of the deviatoric stress ratio $\boldsymbol{r} = \boldsymbol{s}/p$, and can then be visualized either as a sphere with center $\boldsymbol{\alpha}$ and radius $\sqrt{2/3}m$ in the $\boldsymbol{r}$ space, or equivalently as a circular cylinder with same radius and axis along $\boldsymbol{\alpha}$ in the $\boldsymbol{r}$, $\boldsymbol{\alpha}$ space. The latter visualization is illustrated in Fig. 3 where the trace of the cylinder intersection with the $\boldsymbol{r}$ octahedral space appears as a circle with center $\boldsymbol{\alpha}$ and $\sqrt{2/3}m$ radius. The YS is plotted in this octahedral principal stress ratio plane only for the convenience of the illustration and is not entirely accurate since the principal directions of stress ratio $\boldsymbol{r}$ are not necessarily same as those of the back-stress ratio $\boldsymbol{\alpha}$ or $\boldsymbol{n}$ (the latter along $\boldsymbol{r}-\boldsymbol{\alpha}$), thus, they do not share a common octahedral plane in general; the plane should be considered simply as the deviatoric plane, with no loss of generality and relevance to all equations before and after.

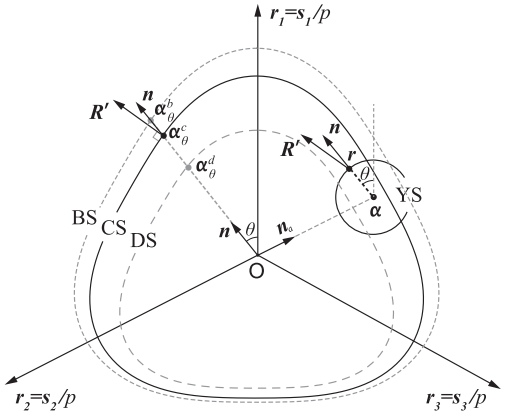

Fig. 3. Illustration of the yield (YS), bounding (BS), dilatancy (DS) and critical state (CS) surfaces on the deviatoric stress ratio space.

The gradient to the yield surface at the current stress is obtained by taking the partial derivative of the function in Eq. (10) with respect to stress as

$$\frac{\partial f}{\partial \boldsymbol{\sigma}} = \boldsymbol{n} - \frac{1}{3}(\boldsymbol{n} : \boldsymbol{r})\boldsymbol{I}; \quad \boldsymbol{n} = \frac{\boldsymbol{r}-\boldsymbol{\alpha}}{\sqrt{2/3}m} \tag{11}$$

where the unit-norm tensor $\boldsymbol{n}$ is the deviatoric part of the gradient of Eq. (11) and it is defined along the direction $\boldsymbol{r}-\boldsymbol{\alpha}$.

3.4. Bounding, dilatancy and critical surfaces

The Bounding Surface (BS), Dilatancy Surface (DS) and Critical State (CS) surface for the back-stress ratio $\boldsymbol{\alpha}$ are defined as three concentric, with respect to the origin, surfaces in the deviatoric space of Fig. 3, shown for convenience as the octahedral plane of the deviatoric stress ratio $\boldsymbol{r}$ as explained in the previous subsection. Their geometrical determination is obtained by three "image"

points, the $\boldsymbol{\alpha}_\theta^b$, $\boldsymbol{\alpha}_\theta^d$ and $\boldsymbol{\alpha}_\theta^c$ defined by "mapping" on them the current back-stress ratio $\boldsymbol{\alpha}$, as the intersection of a line along the direction of $\boldsymbol{n}$ emanating from the origin at a Lode angle θ, as shown in Fig. 3. The corresponding analytical expressions are:

$$\boldsymbol{\alpha}_\theta^b = \sqrt{\frac{2}{3}}\left[g(\theta)M_c exp(n^b < -\zeta >) - m\right]\boldsymbol{n} = \alpha_\theta^b \boldsymbol{n} \tag{12a}$$

$$\boldsymbol{\alpha}_\theta^d = \sqrt{\frac{2}{3}}\left[g(\theta)M_c exp(n^d \zeta) - m\right]\boldsymbol{n} = \alpha_\theta^d \boldsymbol{n} \tag{12b}$$

$$\boldsymbol{\alpha}_\theta^c = \sqrt{\frac{2}{3}}[g(\theta)M_c - m]\boldsymbol{n} = \alpha_\theta^c \boldsymbol{n} \tag{12c}$$

where M_c is the critical state stress ratio in TC and the definition of the scalar-valued quantities α_θ^b, α_θ^d and α_θ^c is self evident. Notice the subtraction of m in Eqs. (12a)–(12c) because these surfaces are associated with back-stress ratio $\boldsymbol{\alpha}$ rather than stress ratio $\boldsymbol{r}$. Such subtraction was not performed in the illustration of Fig. 2a that refers to stress ratio under triaxial conditions. Since, the CS surface is Lode angle dependent, the interpolation of its aperture for the whole Lode angle θ range is done through the function $g(\theta)$ given by Argyris et al. (1974) as

$$g(\theta) = \frac{2c}{(1+c) - (1-c)cos3\theta}; \quad c = \frac{M_e}{M_c} \tag{13}$$

where M_e is the critical stress ratio in TE and

$$cos3\theta = \sqrt{6}tr\boldsymbol{n}^3 = 3\sqrt{6}det\boldsymbol{n} \tag{14}$$

with $\theta = 0^\circ$ and 60° for TC and TE paths, respectively; *det* implies the determinant.

It is important to observe the effect of fabric tensor on the shape of the three surfaces in Fig. 3 for the adopted framework of ACST. While they are concentric in regards to the origin, they are not homologous because now the ζ is different for each Lode angle θ associated with a choice of $\boldsymbol{n}$ (it will be shown subsequently that the $\boldsymbol{n}'$ that defines A and ζ from Eqs. (2) and (4), depends on $\boldsymbol{n}$). If ψ were used instead of ζ within CST, as in Dafalias and Manzari (2004), the surfaces would have been homologous (each one would be scaled version of the others) because ψ is the same for all θ angles. The plot presented in Fig. 3 is based on a transversely isotropic fabric tensor with axis of rotational symmetry along the principal axis $\boldsymbol{r}_1$. Hence, while the CS surface is symmetric in regard to all three axes (no dependence on ζ), the BS and DS have a symmetry only in regards to the principal axis $\boldsymbol{r}_1$ at $\theta = 0$ (due to rotational symmetry of $\boldsymbol{F}$), along which they are displaced upwards and downwards, respectively, resulting in their asymmetry in regards to the axes $\boldsymbol{r}_2$ and $\boldsymbol{r}_3$. Upon shearing at a specific mode defined by the Lode angle, the BS and DS will eventually collapse onto the fabric independent CS surface at critical state where $\zeta = \psi = 0$, while the critical state fabric tensor is not zero. Thus, fabric anisotropy at CS is related to a fabric independent CS failure surface, a result that seems counterintuitive at first, but is fully compatible with ACST that advocates the same Fabric Anisotropy Variable (FAV) $A = A_c = 1$ at CS, for a given shear mode, no matter at which orientation in regards to the sample this shear mode is applied. This must be contrasted with the failure surface notion of reaching a peak stress ratio for a dense sample after which softening begins, thus inducing "failure" and eventually shear banding. This failure surface is in fact the BS at the moment it is crossed by the ascending stress ratio before its descent during softening after crossing the BS, the latter being clearly function of fabric orientation and mode of shearing via the key FAV $A = \boldsymbol{F} : \boldsymbol{n}$ on which it depends via ζ as per Eqs. (2), (4) and (12a). Hence, a possible formation of a shear band will depend orientation-wise on the fabric dependent failure (bounding) surface, and ultimately on the fabric itself.

3.5. Flow rule

Following the work by Dafalias and Manzari (2004) the Lode angle dependent deviatoric plastic strain rate direction tensor $\boldsymbol{R}'$ is normal to the CS surface at $\boldsymbol{\alpha}_\theta^c$ as shown in Fig. 3, also shown transferred at the current stress ratio point $\boldsymbol{r}$. After considerable algebra $\boldsymbol{R}'$ is analytically given by

$$\boldsymbol{R}' = B\boldsymbol{n} - C\left(\boldsymbol{n}^2 - \frac{1}{3}\boldsymbol{I}\right) \tag{15a}$$

$$B = 1 + \frac{3}{2}\frac{(1-c)}{c}g(\theta)cos3\theta; \quad C = 3\sqrt{\frac{3}{2}}\frac{(1-c)}{c}g(\theta) \tag{15b}$$

Observe from Eq. (15a) that $\boldsymbol{R}'$ and $\boldsymbol{n}$ are coaxial tensors since they share the same eigenvectors but not proportional in general since they do not share the same eigenvalues ($\boldsymbol{R}'$ is identical to $\boldsymbol{n}$ for loading in TC and TE). Thus, the flow rule is non-associative on the deviatoric space. Based on Eqs. (14) and (15a) it is possible to show that $\boldsymbol{n} : \boldsymbol{R}' = B - Ctr\boldsymbol{n}^3 = 1$ (Dafalias and Taiebat, 2016), thus, the resulting term $2G(\boldsymbol{n} : \boldsymbol{R}') = 2G$ in the denominator of the last member of Eq. (7).

It is important to point out here that the non-coaxiality between stress $\boldsymbol{r}$ and plastic strain rate direction $\boldsymbol{R}'$ due to fabric is not addressed, because fabric effects were not introduced in the definition of $\boldsymbol{R}'$ in Eqs. (15a), but they will be introduced in the sequel via A and ζ only in relation to the scalar-valued dilatancy and plastic modulus. This was done on purpose in order to maintain the simplicity of the formulation, as compared to that of other models within ACST but a different constitutive platform not involving kinematic hardening, which introduced the effect of A in the flow rule (Gao et al., 2014; Gao and Zhao, 2015b; 2017b). Underlying this simplification is the fact that such fabric-related non-coaxiality is not as intense and persisting as the one arising due to kinematic hardening (Dafalias et al., 2004), which is taken into account because $\boldsymbol{R}'$ has same eigenvectors as $\boldsymbol{n}$ that according to Eq. (11) are those of $\boldsymbol{r} - \boldsymbol{\alpha}$ instead of $\boldsymbol{r}$ or $\boldsymbol{s}$.

3.6. Kinematic hardening

The kinematic hardening (KH) rate equation for the back stress ratio $\boldsymbol{\alpha}$ is given by:

$$\dot{\boldsymbol{\alpha}} = \langle L \rangle H\left(\boldsymbol{\alpha}_\theta^b - \boldsymbol{\alpha}\right) = \langle L \rangle \tilde{\boldsymbol{\alpha}} \tag{16}$$

with a self evident definition of $\tilde{\boldsymbol{\alpha}}$. Note that the rate of the back stress ratio is proportional to the distance of the current back-stress ratio $\boldsymbol{\alpha}$ from its image on BS $\boldsymbol{\alpha}_\theta^b$, of Eq. (12a), consistent with BS plasticity classical scheme. The quantity H of Eq. (16) is given by:

$$H = \frac{2}{3}\frac{h(e, p, A)}{\langle(\boldsymbol{\alpha} - \boldsymbol{\alpha}_{in}) : \boldsymbol{n}\rangle} \tag{17}$$

where the function $h(e, p, A)$ is given by

$$h = G_0 h_1 exp(h_2 A)(e^{-1} - c_h)^2\left(\frac{p}{p_{at}}\right)^{-1/2} \tag{18}$$

where h_1, h_2, c_h= positive material constants.

The $\boldsymbol{\alpha}_{in}$ in Eq. (17) denotes the value of $\boldsymbol{\alpha}$ at the initiation of a new plastic loading process. The term inside the $< >$ in the denominator of Eq. (17) is responsible for the definition of a new plastic loading process as follows. When it becomes negative or zero it means that the current value of $\boldsymbol{n}$ is directed along an opposite direction to $\boldsymbol{\alpha} - \boldsymbol{\alpha}_{in}$, which on the average indicates the overall direction of recent loading history, thus, signaling a new plastic loading process. Notice, that this can happen not only by unloading-reloading in opposite direction, but also as $\boldsymbol{n}$ changes progressively during continued loading without ever unloading, i.e

without ever having $L<0$. The $<>$ then render the denominator zero, the current $\boldsymbol{\alpha}$ becomes the new updated $\boldsymbol{\alpha}_{in}$ and the new loading process begins with an infinite H that will be shown to result into an infinite value of the plastic modulus for smooth elastic-plastic transition. Observe that in the case of continuous change of $\boldsymbol{n}$ there will be a moment when $(\boldsymbol{\alpha}-\boldsymbol{\alpha}_{in}):\boldsymbol{n}$=0, before it becomes negative, and at that moment the updating of the new $\boldsymbol{\alpha}_{in}$ occurs, without any discontinuity of the value of H that approaches infinity as $(\boldsymbol{\alpha}-\boldsymbol{\alpha}_{in}):\boldsymbol{n}$ approaches zero. Had an unloading taken place by the fact $L<0$ in Eq. (7), it does not mean that in the new loading process with a new $\boldsymbol{n}$, the $\boldsymbol{\alpha}_{in}$ will be necessarily updated to the $\boldsymbol{\alpha}$ existing at the moment of new loading; this will happen only if the new $\boldsymbol{n}$ is such as to yield $(\boldsymbol{\alpha}-\boldsymbol{\alpha}_{in}):\boldsymbol{n}\leq 0$ as with the aforementioned continued loading. This is done in order to avoid an unjustified discontinuity that would be induced had the new loading stress point on the YS been identical or very close to the point of unloading, in which case an updating of $\boldsymbol{\alpha}_{in}$ would have induced with no reason an infinite plastic modulus for an otherwise continued loading process.

3.7. Plastic modulus

From the consistency condition $\dot{f}$, in conjunction with Eqs. (7), (10), (11), and (16), the plastic modulus is $K_p=-(\partial f/\partial\boldsymbol{\alpha}):\tilde{\boldsymbol{\alpha}}$, where $\tilde{\boldsymbol{\alpha}}$ is defined in Eq. (16) and $\partial f/\partial\boldsymbol{\alpha}=-p\boldsymbol{n}$. Thus, the multiaxial generalization of K_p is given by:

$$K_p=pH(\boldsymbol{\alpha}_\theta^b-\boldsymbol{\alpha}):\boldsymbol{n} \tag{19}$$

where H is given by Eq. (17). The effect of updating the $\boldsymbol{\alpha}$ to $\boldsymbol{\alpha}_{in}$ on H, discussed in the previous subsection, transfers via Eq. (19) to K_p. Eq. (19) embodies the most characteristic feature of BS plasticity, namely the dependence of the value of the plastic modulus on the distance of the current back-stress ratio $\boldsymbol{\alpha}$ from its image $\boldsymbol{\alpha}_\theta^b$ on the BS, projected along the loading direction $\boldsymbol{n}$. The K_p can become first zero and immediately afterwards negative (softening response), when the $\boldsymbol{\alpha}$ moves outside the BS due to the fact $\boldsymbol{\alpha}_\theta^b$ depends on ζ as per Eq. (12a) and such dependence can cause a shrinking of the BS as ζ becomes less negative due to dilation that reduces the absolute value of ψ in Eq. (4), a notion first proposed by Manzari and Dafalias (1997) in their CST-based two-surface model.

3.8. Dilatancy

The dilatancy D is proportional to the distance of the current back-stress ratio $\boldsymbol{\alpha}$ from the image $\boldsymbol{\alpha}_\theta^d$ on DS, projected along the direction of $\boldsymbol{n}$, Fig. 3. This leads to the definition

$$D=A_d\left(\boldsymbol{\alpha}_\theta^d-\boldsymbol{\alpha}\right):\boldsymbol{n} \tag{20}$$

where $\boldsymbol{\alpha}_\theta^d$ is given by Eq. (12b). The term A_d is in general a function of state variables which in the simplest case can be a constant $A_d=A_0$, adopted in the present work. Notice that Dafalias and Manzari (2004) used a A_d dependent on a fabric-dilatancy tensor (different than the current $\boldsymbol{F}$) to simulate cyclic mobility and liquefaction, however, this is out of the scope of this work.

Recall the very important dependence of α^d on the DSP ζ according to Eq. (12b), that embodies the fundamental effect of fabric anisotropy on dilatancy. It is instructive to demonstrate the foregoing effect by a thought experiment viewed from the two different perspectives of classical CST and ACST. Consider first CST where ψ substitutes for ζ in all preceding expressions. Assume that a specimen with TC-like fabric tensor is under hydrostatic pressure p and has a $\psi=e-e_c<0$, i.e. it is denser than critical, thus, its e, p state is plotted as a point below the CSL in $e-p$ space, Fig. 2b. Then consider loading the specimen in TC ($g(\theta)=1$) and TE ($0<g(\theta)=c<1$); in either case ψ is same and negative, therefore the $g(\theta)M_c\exp(n^d\zeta)-m<g(\theta)M_c-m$, and correspondingly, based on Eqs. (12b) and (12c) the $\boldsymbol{\alpha}_\theta^d:\boldsymbol{n}<\boldsymbol{\alpha}_\theta^c:\boldsymbol{n}$. The dilatancy D of Eq. (20) will begin with a positive value (contraction) for low $\boldsymbol{\alpha}:\boldsymbol{n}$, since $\boldsymbol{\alpha}_\theta^d:\boldsymbol{n}>\boldsymbol{\alpha}:\boldsymbol{n}$ but eventually will become negative ($\boldsymbol{n}$ remains constant in monotonic TC or TE) when the increasing $\boldsymbol{\alpha}:\boldsymbol{n}$ becomes greater than $\boldsymbol{\alpha}_\theta^d:\boldsymbol{n}$ (still less than $\boldsymbol{\alpha}_\theta^c:\boldsymbol{n}$). At that point, $D<0$, thus the sample will dilate till eventual CS failure where $\boldsymbol{\alpha}_\theta^d:\boldsymbol{n}=\boldsymbol{\alpha}_\theta^c:\boldsymbol{n}$ as per Eqs. (12b) and (12c) when $\psi=0$ at CS (recall that ψ instead of ζ enters Eqs. (12a)–(12c) within CST). This response will be same for TC and TE because the ψ and the ensuing $\boldsymbol{\alpha}_\theta^d:\boldsymbol{n}<\boldsymbol{\alpha}_\theta^c:\boldsymbol{n}$ are the same for either cases. However, experimental data show that the response of such a sample with a strong TC-like fabric resulting from the preparation method, while indeed is eventually dilative in TC, it is very much contractive in TE. This drastically different response cannot be explained merely by the different Lode angles in TC and TE that imply different M^c values, hence, classical CST cannot offer a plausible explanation and subsequent simulation.

On the other hand ACST can. If the same specimen is loaded in TC, the $0<A=\boldsymbol{F}:\boldsymbol{n}'<1$ (both $\boldsymbol{F}$ and $\boldsymbol{n}'$ are TC-like tensors), while if it is loaded in triaxial extension, the $-1<A=\boldsymbol{F}:\boldsymbol{n}'<0$ because the $\boldsymbol{n}'$ is TE-like (it is the -$\boldsymbol{n}'$ of TC) while the $\boldsymbol{F}$ remains initially TC-like, as illustrated in Fig. 2a and 2b. In either case the second term $-e_A(A-1)$ of Eq. (4) will be positive, but greater in TE than in TC. Therefore, since ψ is the same and negative in both cases, the DSP ζ from Eq. (4) will be algebraically smaller in TC than in TE, and so will be the $\boldsymbol{\alpha}_\theta^d:\boldsymbol{n}$ based on Eq. (12b). In fact with $\psi<0$, it is possible to have $\zeta<0$ in TC and $\zeta>0$ in TE, i.e the e, p point will be located between the two DSL corresponding to $0<A<1$ for TC and $-1<A<0$ for TE (see Fig. 2b), due to the change of the loading direction from $\boldsymbol{n}'$ in TC to -$\boldsymbol{n}'$ in TE. For those signs of ζ, it follows that $\boldsymbol{\alpha}_\theta^d:\boldsymbol{n}<\boldsymbol{\alpha}_\theta^c:\boldsymbol{n}$ in TC and $\boldsymbol{\alpha}_\theta^d:\boldsymbol{n}>\boldsymbol{\alpha}_\theta^c:\boldsymbol{n}$ in TE. Thus, during shearing in TC $\boldsymbol{\alpha}:\boldsymbol{n}$ will eventually become greater than $\boldsymbol{\alpha}_\theta^d:\boldsymbol{n}$ and dilation will take place since $D<0$, according to Eq. (20). To the contrary, in TE the $\boldsymbol{\alpha}:\boldsymbol{n}$ will remain smaller than $\boldsymbol{\alpha}_\theta^d:\boldsymbol{n}>\boldsymbol{\alpha}_\theta^c:\boldsymbol{n}$ and continuous contraction will take place since $D>0$ based on Eq. (20); such contraction can in fact be strong enough to lead the sample to static liquefaction under undrained shearing, or close to it, in TE. This is exactly the experimental response observed in Yoshimine et al. (1998) and shown later in the simulations.

Finally, if the back stress-ratio is written as $\boldsymbol{\alpha}=\alpha\boldsymbol{n}_\alpha$ with α the norm and $\boldsymbol{n}_\alpha$ the unit-norm deviatoric direction of $\boldsymbol{\alpha}$ as shown in Fig. 3, one can re-write Eq. (20) as $D=A_0\left(\alpha_\theta^d-\alpha\boldsymbol{n}_\alpha:\boldsymbol{n}\right)$. With a very small value of m in Eq. (10), the stress ratio $\boldsymbol{r}$ and back stress ratio $\boldsymbol{\alpha}$ are very close to each other, while recall that $\boldsymbol{n}$ has same eigenvectors as the direction of the deviatoric plastic strain rate $\boldsymbol{R}'$ from Eqs. (15a). Hence, the scalar term $\boldsymbol{n}_\alpha:\boldsymbol{n}$ in the foregoing expression of D reflects a measure of the non-coaxiality between the stress and the plastic strain rate. This is reminiscent of the non-coaxiality coefficient introduced by Gutierrez and Ishihara (2000) based on a dissipation assumption, and appears automatically in a BS formulation with KH via the term $\boldsymbol{n}_\alpha:\boldsymbol{n}$ because of the projection of the distance $\boldsymbol{\alpha}_\theta^d-\boldsymbol{\alpha}$ on $\boldsymbol{n}$ in Eq. (20).

3.9. Evolution of fabric tensor

The evolution of the fabric tensor $\boldsymbol{F}$ is given by

$$\dot{\boldsymbol{F}}=\langle L\rangle c_0 exp(A)(\boldsymbol{n}'-r\boldsymbol{F}) \tag{21}$$

where recall that $\boldsymbol{n}'$ is the unit norm tensor along the plastic strain rate direction $\boldsymbol{R}'$. The variable $r\leq 1$ was introduced in ACST by Li and Dafalias (2012) in order to allow the norm F to acquire values >1 for dense samples before reaching the value of 1 at CS, where also the $r=1$. However, in our present applications it was found

that such variable r does not change significantly the response, and in view of insufficient data for the norm of the fabric tensor it was decided to use the default value $r = 1$ in all subsequent simulations. The $exp(A)$ is an additional term compared to the original proposition in Li and Dafalias (2012), based on the suggestion in Papadimitriou et al. (2014) where $exp(kA)$ was used (it is found that k=1 is a good default value for the present work) in order to enhance the pace of fabric evolution when larger A values are encountered.

Following Li and Dafalias (2012), one can decompose Eq. (21) into the rate of the norm F, and the rate of the unit-norm direction $\boldsymbol{n}_F$ as

$$\dot{F} = \langle L \rangle c_0 exp(A)(N - rF) \tag{22a}$$

$$\dot{\boldsymbol{n}}_F = \langle L \rangle \left[\frac{c_0 exp(A)}{F} \boldsymbol{n}' - N \boldsymbol{n}_F \right] \tag{22b}$$

recalling that $N = \boldsymbol{n}_F : \boldsymbol{n}'$. Observe that the factor r, in front of the norm of the fabric tensor in Eq. (22a), does not appear in Eq. (22b) that addresses the "direction" of it. Notice also that when $F = 0$ (isotropic fabric) at the denominator of Eq. (22b) one must use the basic equation for the rate of $\boldsymbol{F}$ given by Eq. (21).

3.10. Triaxial formulation

A very brief summary of the SANISAND-F formulation in triaxial $p - q$ space is presented here. The model's formulation follows the work presented in Li and Dafalias (2012) and the equations are extended to include kinematic hardening with a very small yield surface, following the triaxial formulation of the two-surface model presented in Dafalias and Manzari (2004). The present section is useful to those readers who would like to have a very simple formulation for testing and calibrating the model under triaxial conditions coaxial with the fabric anisotropy, as was discussed in previous sections. It should be mentioned that in Li and Dafalias (2012) the triaxial formulation was applied for simulating the response under various orientations of the stress in regards to the fabric under the disclaimer of relative inaccuracy because in such cases of fabric anisotropy not being coaxial with the stress, the response necessarily cannot be triaxial, hence, it cannot be described by a triaxial formulation. This is remedied in the present paper with the multiaxial formulation presented earlier.

In triaxial stress space, the deviatoric stress is given by $q = \sigma_1 - \sigma_3$ and the mean effective stress by $p = (\sigma_1 + 2\sigma_3)/3$, where σ_1 and σ_3 are the axial σ_z and radial σ_r principal effective stresses, respectively; notice that here the σ_1 is not necessarily the major principal stress as in the HCA definition, thus, q may acquire negative values in triaxial extension when $\sigma_1 < \sigma_3$. The deviatoric shear strain is given by $\varepsilon_q = (2/3)(\varepsilon_1 - \varepsilon_3)$, while the volumetric strain is given by $\varepsilon_v = \varepsilon_1 + 2\varepsilon_3$, where again ε_1 and ε_3 are the axial ε_z and radial ε_r principal strain values, respectively. Similarly to q, the ϵ_q takes negative values in triaxial extension, when $\varepsilon_1 < \varepsilon_3$. The stress ratio is defined as $\eta = q/p$. The additive decomposition of the total strain rate into elastic and plastic parts is assumed, denoted by superscripts e and p respectively. The SANISAND-F equations formulated in triaxial space are summarized in Table 1.

Following the approach in the Appendix of Dafalias and Manzari (2004), and denoting by a superscript $(^*)$ triaxial quantities, one can show from Eqs. (19), (17) and the equation of K_p^* in Table 1, that $K_p = (2/3)K_p^*$, because of the addition of the factor 2/3 in Eq. (17) for H, as it should from the relation between triaxial and multiaxial formulations. Hence, the term h is given by the same Eq. (18) in either Eq. (17) for multiaxial space or in its triaxial equivalent H^* in Table 1. One can also show from Eq. (20) and the equation of D^* in Table 1 that $D = \sqrt{2/3}D^*$, as it should from the definition of dilatancy in multiaxial and triaxial formulations, hence, the constitutive parameter A_d is same for D as formulated in triaxial and multiaxial space. This allows the use of the simpler and cost-efficient in terms of computational power triaxial model for the calibration of the multiaxial SANISAND-F model solely based on drained and undrained triaxial experiments (see Section 4.1).

Table 1
Constitutive ingredients of the SANISAND-F model as formulated in the triaxial stress space.

Description	Equation
CSL in $e - p$	$e_c = \hat{e}_c(p) = e_{ref} - \lambda_c (p/p_{at})^{\xi}$
Elastic Shear Modulus	$G = G_0 p_{at} \frac{(2.97-e)^2}{1+e} \left(\frac{p}{p_{at}}\right)^{1/2}$
Elastic Bulk Modulus	$K = \frac{2(1+\nu)}{3(1-2\nu)} G$
Yield surface	$f = \lvert q - p\alpha \rvert - pm = 0$
Bounding Surface	$a^b = M^c exp(n^b < -\zeta >) - m$
Dilatancy Surface	$a^d = M^c exp(n^d \zeta) - m$
CS Surface	$a^c = M^c - m$
Plastic Modulus	$K_p^* = pH^* \left(\alpha^b \mp \alpha\right)$
	$H^* = \frac{h(e,p,A)}{\lvert \alpha - \alpha_{in} \rvert}$
	$h = G_0 h_1 \exp(h_2 A)(e^{-1} - c_h)^2 \left(\frac{p}{p_{at}}\right)^{-1/2}$
Dilatancy	$D^* = A_d (a^d \mp a)$
Fabric Evolution	$\dot{F} = c_0 \exp(A)(N - rF) \lvert \dot{\varepsilon}_q^p \rvert$

4. Calibration and validation

4.1. Calibration process

The SANISAND-F model has a total of 17 non-negative model constants. Their calibration for Toyoura sand has been performed with the use of the undrained triaxial compression (UTC) and extension (UTE) tests of Yoshimine et al. (1998) and the drained triaxial compression (DTC) tests of Verdugo and Ishihara (1996). The foregoing conventional laboratory tests are ideal for calibration purposes, since they are both drained and undrained, they cover a significant range of initial conditions (initial p = 50–500 kPa and e = 0.81–0.96) and they include both TC and TE tests, i.e. the extreme cases of anisotropy effects for samples with a horizontal deposition plane. The list of model constants, their nature and the equations in which they appear in the model formulation are presented in Table 2, along with their values for Toyoura sand.

Out of the 17 model constants, 4 are directly related to fabric dependence (F_{in}, e_A, h_2, c_0), 2 are indirectly related to it (n^b, n^d), while the remaining 11 are essentially identical to the constants of any SANISAND model from the literature that is not built

Table 2
Material constants of SANISAND-F model, constitutive equations in which they appear and their values for Toyoura sand.

Description	Symbol	Values	Equation
Elasticity	G_0	125	(9)
	ν	0.05	(9)
Critical state	e_{ref}	0.934	(8)
	ξ	0.7	(8)
	λ	0.019	(8)
	M_c	1.25	(12a)–(12c)
	c	0.75	(13)
Plastic modulus	h_1	7.5	(18)
	c_h	0.85	(18)
	n^b	1.4	(12a)
Yield surface	m	0.01	(10)
Dilatancy	A_0	0.704	(20)
	n^d	3.5	(12b)
Fabric	e_A	0.0818	(4)
	F_{in}	0.5	(-)
	c_0	5.2	(21)
	h_2	1.3	(18)

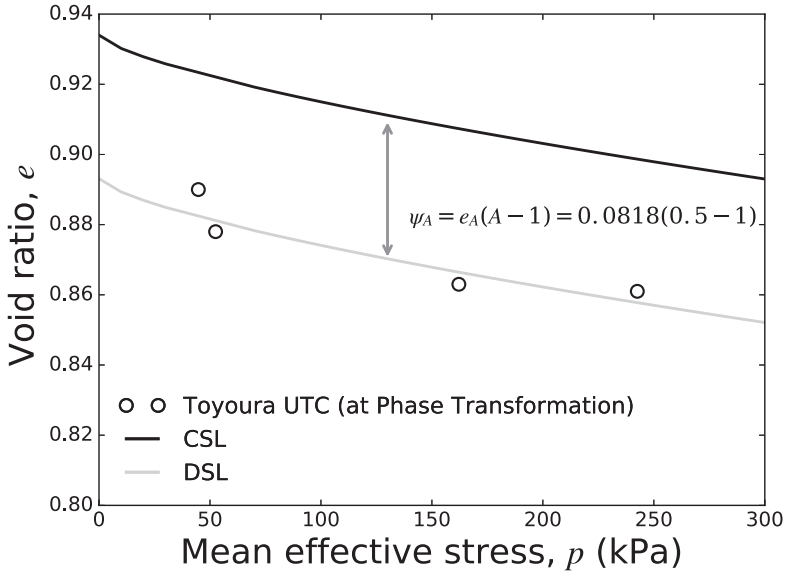

Fig. 4. Calibration of model constant e_A in terms of undrained triaxial compression tests. Data after Yoshimine et al. (1998).

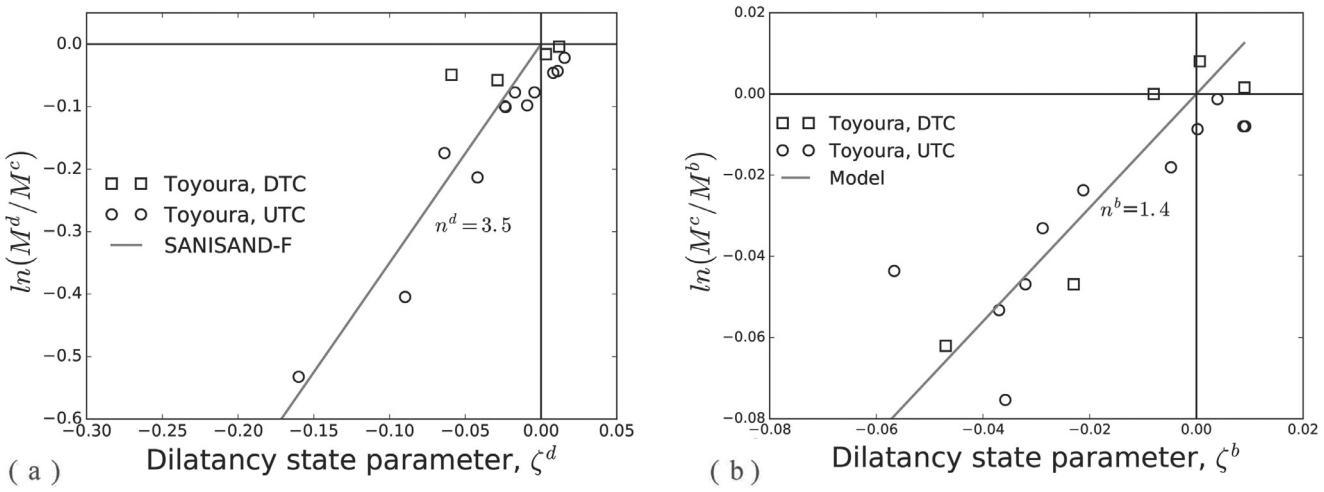

Fig. 5. Calibration of model constants n^b and n^d in terms of undrained and drained triaxial compression tests. UTC data after Yoshimine et al. (1998) and DTC data after Verdugo and Ishihara (1996).

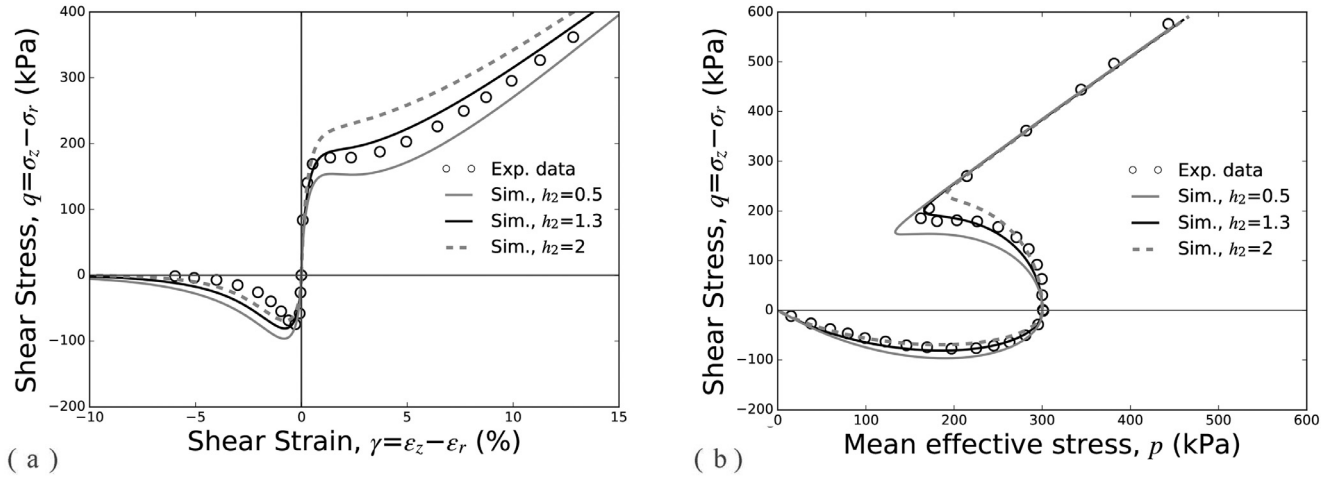

Fig. 6. Calibration of model constant h_2 in terms of undrained triaxial compression and extension data. Data after Yoshimine et al. (1998).

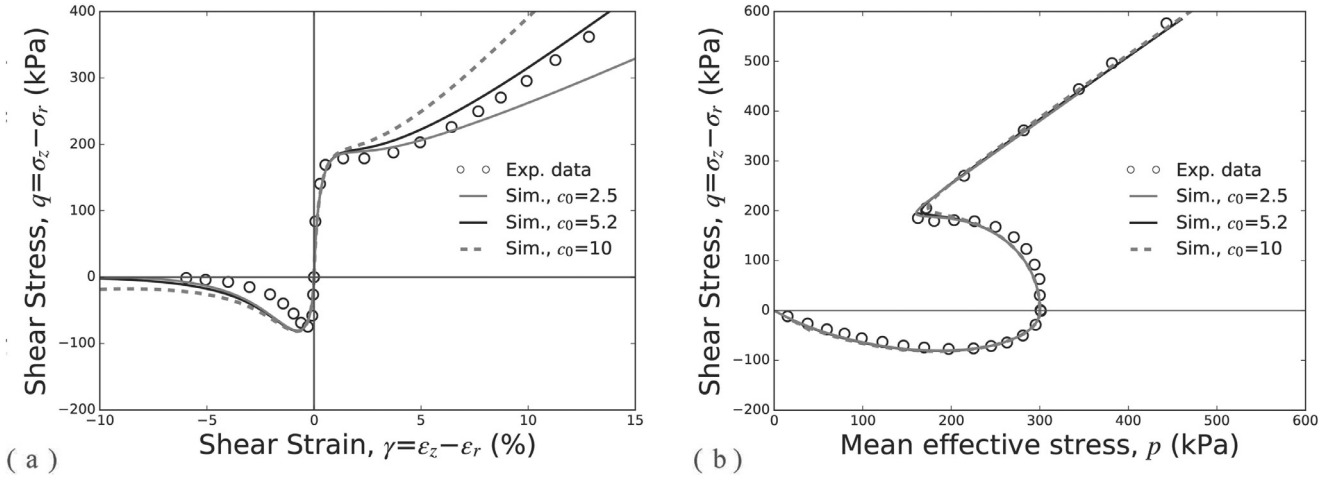

Fig. 7. Calibration of model constant c_0 in terms of undrained triaxial compression and extension data. Data after Yoshimine et al. (1998).

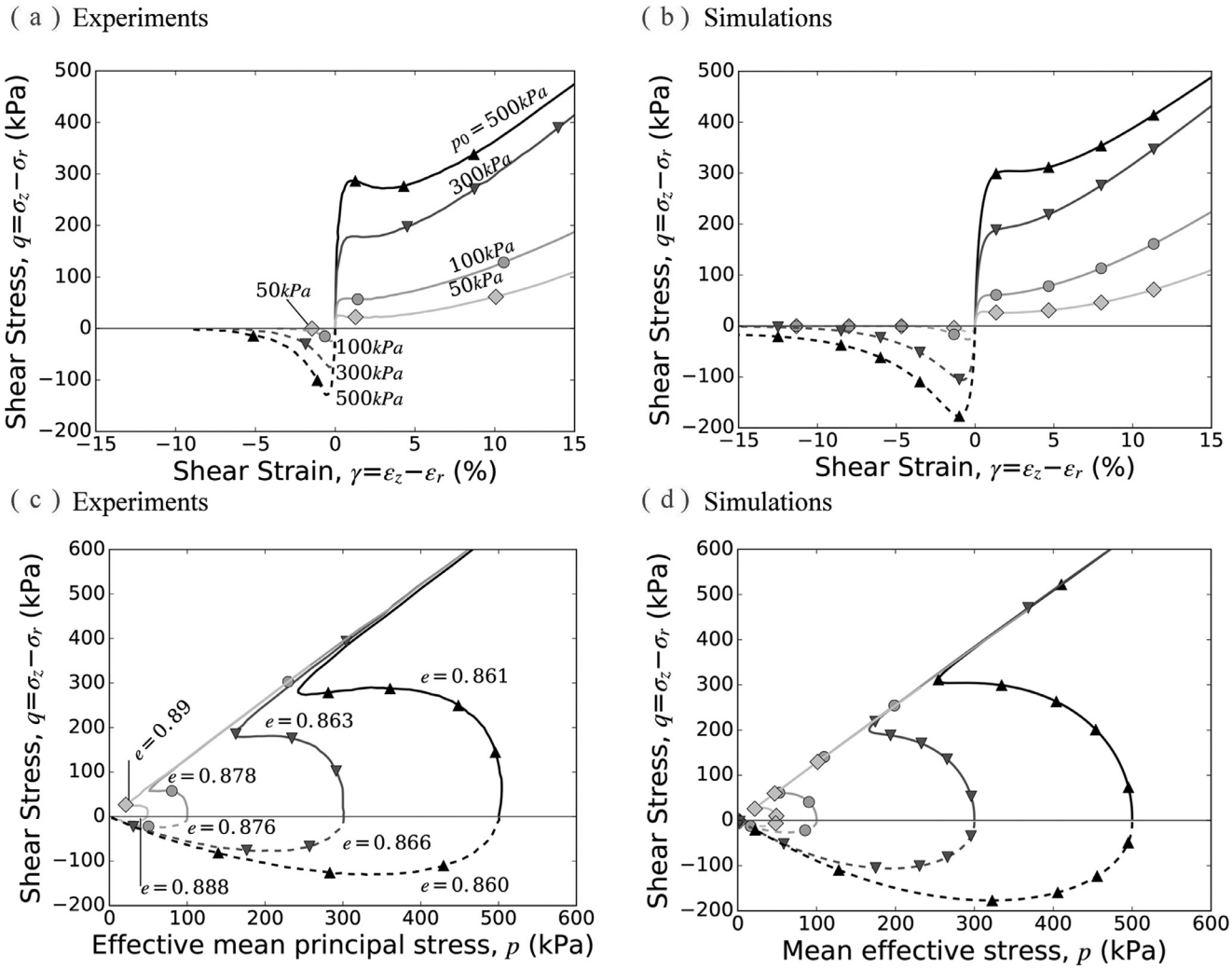

Fig. 8. Experimental data (a, c) and SANISAND-F simulations (b, d) for undrained triaxial compression ($b=0$, $\alpha_\sigma=0$) and extension ($b=1$, $\alpha_\sigma=90^\circ$) loading on Toyoura sand with different void ratios and stress levels. Data after Yoshimine et al. (1998).

within the premises of ACST. In regards to these 11 typical model constants, note that the 2 elasticity constants (G_0, ν), the 5 critical state constants (M_c, c, e_0, λ, ξ) and the size of the small yield surface m have the exact same value and meaning as in Dafalias and Manzari (2004), who also calibrated their two-surface model for Toyoura sand. Sole exception is c which was increased to 0.75 (from 0.712) for better simulation of extension paths. In addition, the constants h_1 and c_h that scale the plastic modulus K_p and the A_0 that controls the dilatancy D of the model have the same operation as in Dafalias and Manzari (2004), but also in many bounding

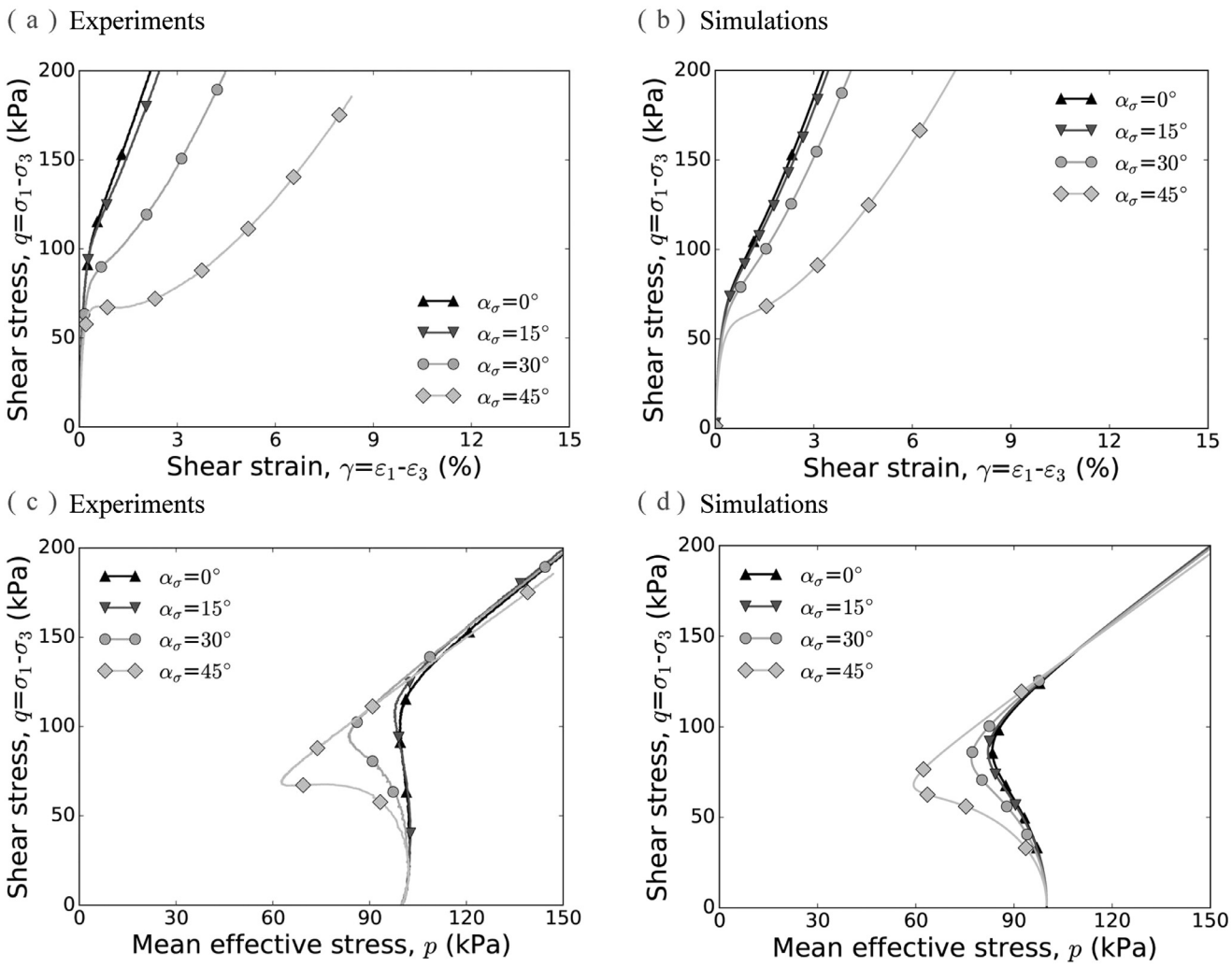

Fig. 9. Experimental data (a, c) and SANISAND-F simulations (b, d) for undrained shearing with constant $b = 0$ and constant $\alpha_\sigma = 0^\circ - 45^\circ$ on Toyoura sand with $e = 0.82$–0.829. Data after Yoshimine et al. (1998).

surface models that are within the SANISAND family (e.g. Loukidis and Salgado, 2009; Taiebat and Dafalias, 2008). Nevertheless, their values in Table 2 are not identical to those in Dafalias and Manzari (2004), since the K_p and D are model ingredients that are hereby related to fabric dependence, thus affecting the values they take for Toyoura sand. Further details for the calibration of the classical SANISAND parameters are thoroughly discussed in many relevant publications (e.g. Dafalias and Manzari, 2004; Loukidis and Salgado, 2009; Taiebat and Dafalias, 2008) and need not be repeated here. What is discussed here in detail is the calibration of the 6 fabric-related model constants in a systematic and complete presentation that is missing from previous works on constitutive models formulated within the ACST.

Specifically, the first action is the initialization of the fabric tensor. For a sand sample prepared by any method (pluviation, tamping, etc.) along the vertical z axis and having an $r\theta$ horizontal plane of deposition, where r the radial and θ the circumferential axes as in Fig. 1, the ensuing transverse isotropy is characterized by the initial value of the norm of the fabric tensor $\boldsymbol{F}$, denoted by F_{in}, and the principal values of its unit-norm direction $\boldsymbol{n}_F$, namely $n_{Fzz} = n_{F1} = 2/\sqrt{6}$ and $n_{Frr} = n_{F\theta\theta} = n_{F2} = n_{F3} = -1/\sqrt{6}$. This F_{in} reflects the initial fabric anisotropy intensity, whose measurement is still a current research endeavor. Existing efforts in this direction include small strain measurements in different directions (e.g. via bender element testing) or measurement in the laboratory via X-ray computed tomography (e.g. Andò et al., 2013). From another point of view, Zhao and Gao (2015) proposed the quantification of F_{in} based on the value of dq/dp at the very beginning of an undrained triaxial test following isotropic consolidation. In this work we use a value of $F_{in} = 0.5$, which is very close to what was inferred by Zhao and Gao (2015) (F_{in} =0.47), within the range of $F_{in} = 0$ - 0.6 for Toyoura sand for different preparation methods (Zhao and Gao, 2015) and the same with that used in Papadimitriou et al. (2018).

Then, constant e_A is estimated, that determines the parallel downward displacement of the Dilatancy State Line (DSL) with respect to the Critical State Line (CSL) in the $e - p$ space, as shown in Fig. 2b. An appropriate value of e_A is estimated using at least 2 UTC tests at different void ratios, by plotting their p values at phase transformation in the $e - p$ space. This is performed in Fig. 4, where the UTC tests of Yoshimine et al. (1998) are used for calibration. Based on Eq. (4), the displacement of the DSL with respect to the CSL is given by the quantity $\psi_A = e_A(A - 1)$, whose negative sign implies downward displacement. For a sand sample prepared by any preparation method, a loading in TC implies $N = 1$ in Eq. (2), hence the quantity $\psi_A = e_A(F - 1)$ where F the norm of the fabric tensor. By assuming that $F = F_{in}$ (= 0.5 from above), a value of $e_A = 0.0818$ gives a good fit of the data in Fig. 4. In passing notice that norm F increases during the UTC tests, but since phase

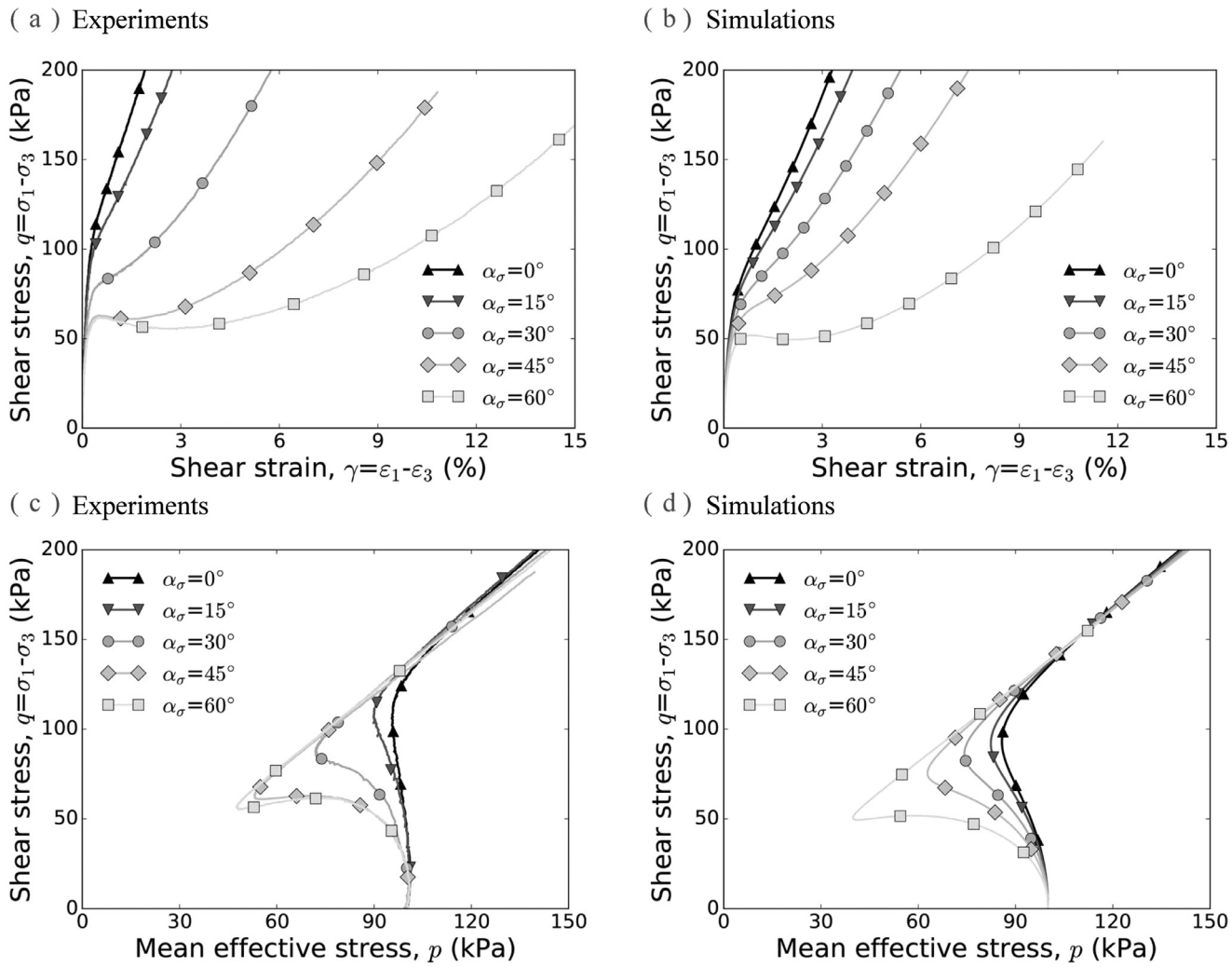

Fig. 10. Experimental data (a, c) and SANISAND-F simulations (b, d) for undrained shearing with constant $b = 0.25$ and constant $\alpha_\sigma = 0^\circ - 60^\circ$ on Toyoura sand with $e = 0.813$–0.818. Data after Yoshimine et al. (1998).

transformation is reached after relatively small strain, assuming that F still retains its initial value of F_{in} (= 0.5) is a satisfactory approximation for the calibration of e_A.

The model constants n^b and n^d are related to the values of the deviatoric stress ratio η at the peak, M^b, and at phase transformation, M^d, respectively. Particularly, based on the equations for the bounding and dilatancy back-stress ratios α^b and α^d (see Table 1), these two constants can be calculated for the special case of triaxial loading conditions, as follows:

$$n^b = \frac{ln\left(M^c/M^b\right)}{\zeta^b}; \quad n^d = \frac{ln\left(M^d/M^c\right)}{\zeta^d} \tag{23}$$

Hence, their estimation is based on the values of M^c, M^b and M^d measured from DTC and UTC tests, as well as the values of DSP ζ at the peak, ζ^b, and at phase transformation, ζ^d. For their calibration, the DTC tests of Verdugo and Ishihara (1996) and the UTC tests of Yoshimine et al. (1998) were used, whose data are plotted in Fig. 5(a) and (b) for n^d and n^b, respectively. Based on these figures, the employed calibration data are satisfactorily fitted by n^b = 1.4 and n^d = 3.5. It should be underlined here that the values of ζ^b and ζ^d included in Eq. (23) are not equal to the initial values of the DSP ζ, but to the values of ζ when $\eta = M^b$ and $\eta = M^d$, respectively. Based on Eq. (2), their estimation requires the CSL line in the $e - p$ space, the value of e_A (from above) and the values of e, p and FAV A at those instances. While e and p are directly measured from the data, the pertinent value of A requires estimation. Since TC tests on sand samples with a horizontal deposition plane are employed for calibration, N=1 applies and hence $A = F$ throughout these tests. However, sand fabric (and hence the norm F of the fabric tensor) evolves with strain. Additionally, attaining phase transformation (dilatancy stress ratio), where $\eta = M^d$, requires smaller strain than what is required to attain the peak stress ratio, where $\eta = M^b$, and much smaller strain than what is required to reach CS. In order to take this effect into account, the F was considered equal to 0.70 and 0.90 (i.e. larger than F_{in} = 0.5, but smaller than F_c=1 at CS) for the estimation of ζ^d and ζ^b, respectively, in all calibration tests included in Fig. 5.

Finally, the h_2 that enters the plastic modulus K_p equation and the c_0 that scales the rate equation of fabric evolution have to be calibrated, and this is performed with trial-and-error runs. Both of these constants are related to the relative difference in the sand response under widely different loading directions and values of A, when starting from the same initial conditions. For this purpose, ideal are the UTC and UTE tests of Yoshimine et al. (1998), of which the 2 respective tests with initial p=300 kPa and e=0.86 were selected. In Fig. 6 the effective stress paths and the stress-strain relation of these 2 tests are presented, along with their simulations with the values of model constants in Table 2, as well as with

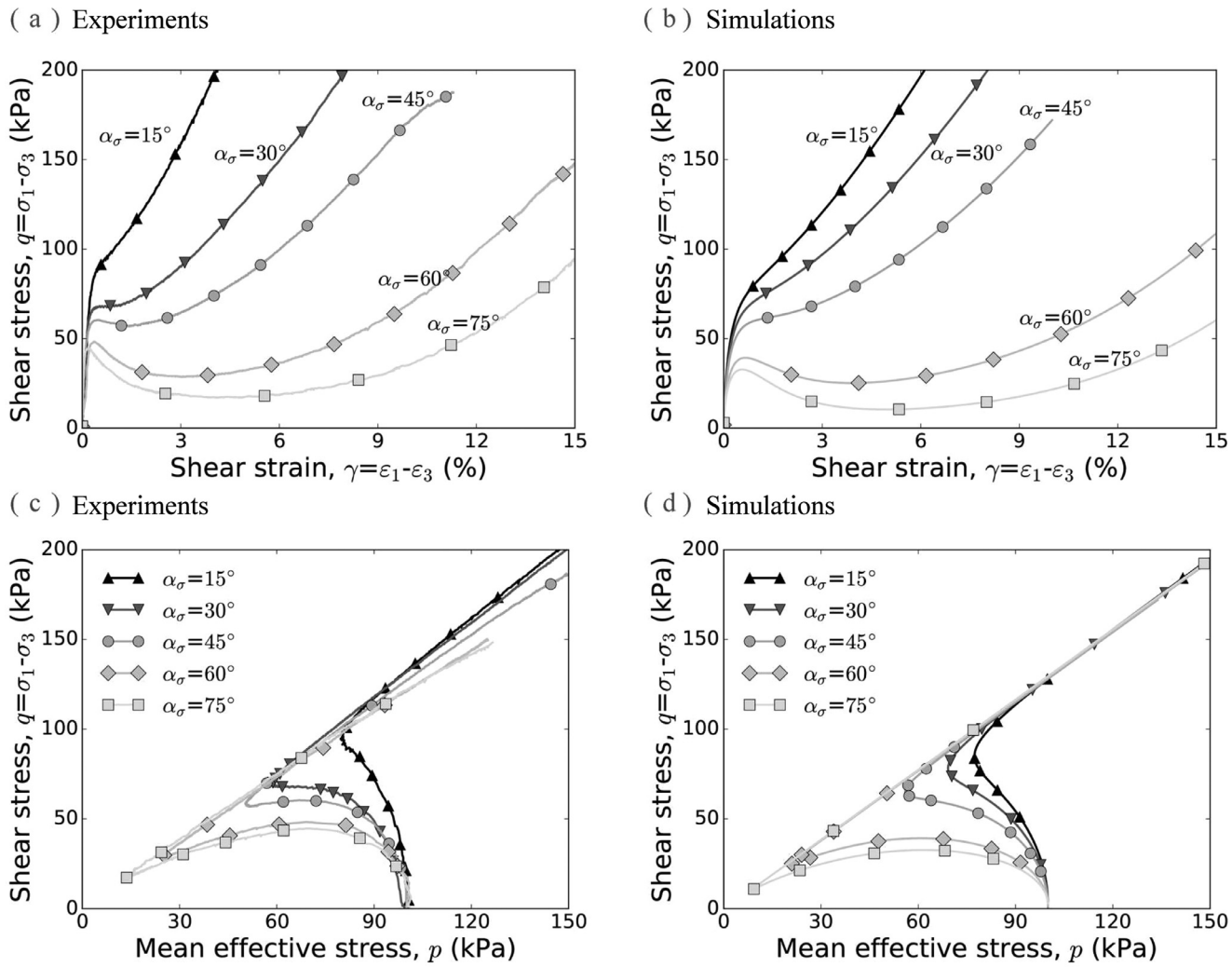

Fig. 11. Experimental data (a, c) and SANISAND-F simulations (b, d) for undrained shearing with constant $b = 0.5$ and constant $\alpha_\sigma = 15° - 75°$ on Toyoura sand with $e =$ 0.821–0.828. Data after Yoshimine et al. (1998).

slightly higher and lower values of the h_2 constant. Fig. 7 presents a similar sensitivity analysis for the same data, but with simulations where the value of c_0 is varied in comparison to its value in Table 2. These figures show that an increase of h_2 leads to enhanced anisotropic effects on the sand response, while an increase of c_0 results in faster fabric evolution towards its critical state value and hence stiffer response for both TC and TE.

In terms of procedure, the calibration initiates from the 13 model constants that do not require trial-and-error runs, starting from G_0 and ν (elasticity), the M_c, c, e_0, λ, ξ (critical state), the dilatancy constant A_0 and the selection of the yield surface size m. Then, the first fabric-related constants are pinpointed, starting from the selection of F_{in}, the estimation of e_A (in Fig. 4) and the calculation of n^b and n^d (in Fig. 5). In the sequel, the 4 remaining model constants, namely h_1, c_h, h_2, c_0, requiring trial-and-error runs are calibrated. The calibration procedure targets first h_1 and c_h on the basis of simulation of at least two TC tests starting from different void ratios. In order to perform these runs, one sets h_2=1 and c_0=5 as good average values for any sand and employs the already depicted values for the directly calibrated other 13 constants. This simulation step will provide a first pair of h_1 and c_h values, which will then be used (along with the 13 directly calibrated model constants) for performing trial and error runs for pinpointing a better pair of h_2 and c_0 values for a duet of TC and TE tests starting from the same initial conditions (as in Figs. 6 and 7). If needed, a final round of trial-and-error runs is performed for all employed calibration tests in order to finalize the optimal values for these 4 model constants, while retaining the 13 directly calibrated model constants fixed.

In conclusion, the SANISAND-F model has 17 model constants, out of which only 4 require a trial-and-error calibration process. This number is not considered excessive, especially if one considers the straightforward calibration procedure outlined above that requires only conventional TC and TE tests. This advantage of the model is underlined by its capabilities, as explored in the next section that presents satisfactory simulations of 55 different tests on differently prepared Toyoura sand samples undergoing different modes of shearing, but simulated with the same set of model constants outlined in Table 2.

4.2. Model validation

In this section, the validation of the proposed model by simulating experimental data collected from the literature is presented. More specifically, undrained and drained shearing tests performed with the use of hollow cylinder apparatus (HCA) are simulated, with constant intermediate principal stress parameter b and constant orientation angle of stress principal axes (PA) α_σ, with

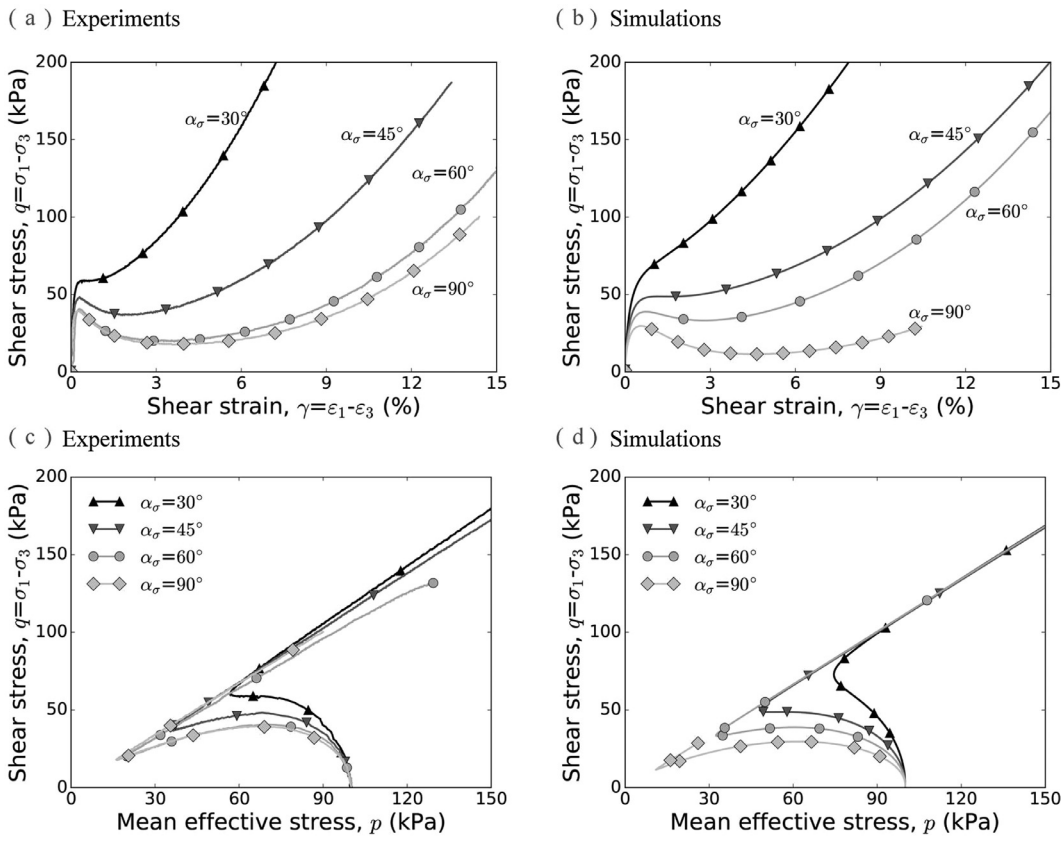

Fig. 12. Experimental data (a, c) and SANISAND-F simulations (b, d) for undrained shearing with constant $b = 0.75$ and constant $\alpha_\sigma = 30^\circ - 90^\circ$ on Toyoura sand with $e = 0.817$–0.830. Data after Yoshimine et al. (1998).

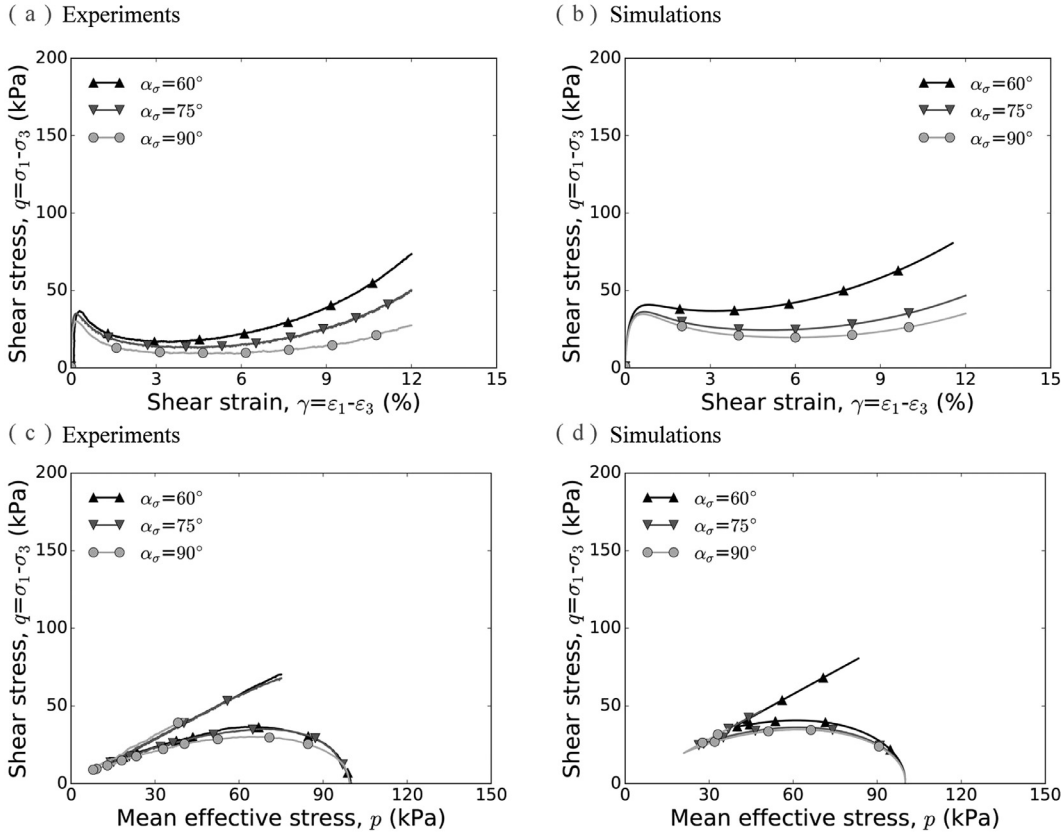

Fig. 13. Experimental data (a, c) and SANISAND-F simulations (b, d) for undrained shearing with constant $b = 1$ and constant $\alpha_\sigma = 60^\circ - 90^\circ$ on Toyoura sand with $e = 0.825$–0.826. Data after Yoshimine et al. (1998).

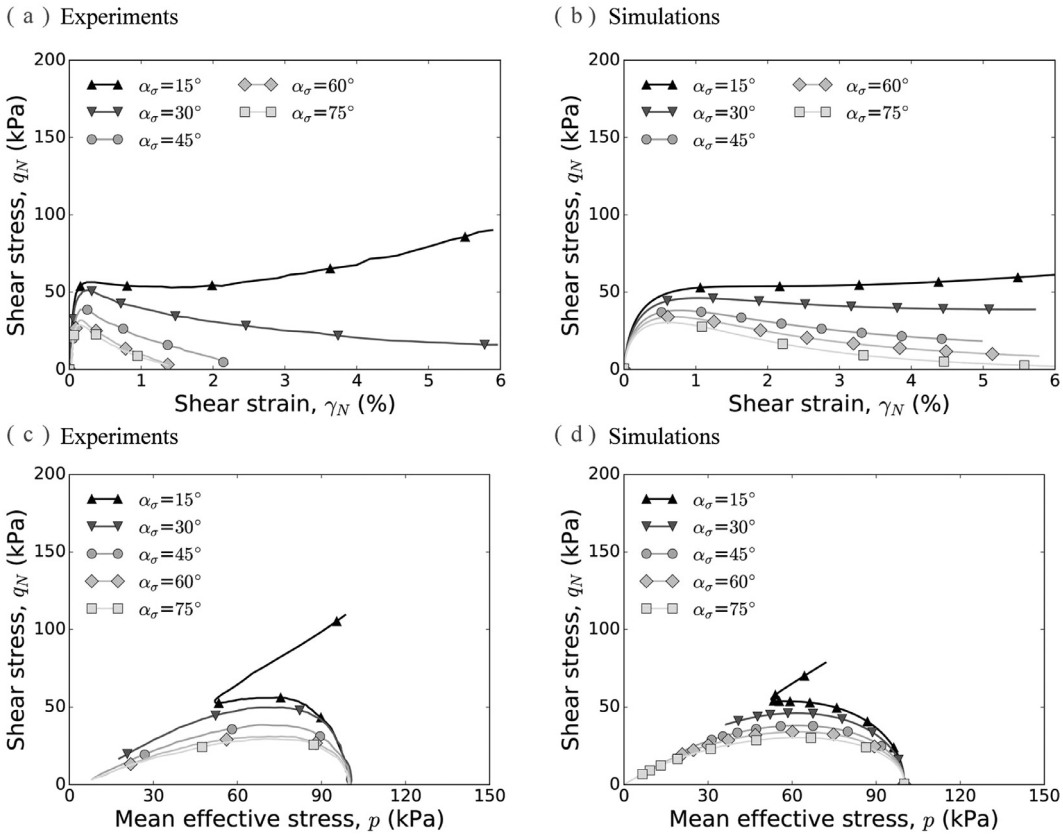

Fig. 14. Experimental data (a, c) and SANISAND-F simulations (b, d) for undrained shearing with constant $b = 0.5$ and constant $\alpha_\sigma = 15^\circ - 75^\circ$ on Toyoura sand with $D_r \approx 30\%$, $e = 0.859$–0.867. Data after Nakata et al. (1998).

respect to the vertical z-axis in the $z-\theta$ plane. A wide range of values for void ratio e, b parameter, mean effective stress p and angle α_σ are investigated.

Fig. 8 presents the undrained response of Toyoura sand under TC and TE. The difference in both the experimentally observed stress-strain response and stress path, for specimens with the same initial p and almost identical void ratios e is huge. The model is capable of reproducing the much softer and contractive response in TE compared to TC, due to the fact that the evolving anisotropy is taken into account through the fabric dependent formulation; the accuracy of the simulation results is high, with the same set of values for the model constants in all the simulations. The reader is referred to the detailed explanation of such difference given after Eq. (20) based on the different values of A and consequently of ζ in TC and TE. In passing notice that that the tests shown in Fig. 8 were used for calibration purposes and the dramatic difference in the undrained response between TC and TE reflects both the different b and α_σ values in these two type of tests (TC: $b = 0$, $\alpha_\sigma = 0^\circ$; TE: $b = 1$, $\alpha_\sigma = 90^\circ$). Thus, a thorough investigation for the whole range of b and α_σ values is needed. It is important to highlight that all the simulations in the sequel are performed with the same set of model constants established by the TC and TE calibration simulations of Fig. 8, without tuning them for different stress paths.

Figs. 9–13 present the experimental data and simulation results for undrained torsional shearing of Toyoura sand for the full range of b and α_σ values; the data are after (Yoshimine et al., 1998). Each figure consists of a series of tests with the same b value ($b = 0$, $b = 0.25$, $b = 0.5$ and $b = 1$) and various α_σ angles. Changing α_σ implies that the direction of the applied stress with respect to the fabric is different while the b-values remain same for all tests in each series. The trend of the response to become softer and more contractive with an increased α_σ for each series, is well reproduced by the model. The difference of the response of the material for the same stress loading history but different orientation of the stress principal axes in regards to the fabric, is indeed extraordinary. For example in Fig. 11a, for b=0.5 the deviatoric stress q values at deviatoric strain γ of about 5% for $\alpha_\sigma = 15^\circ$ and $\alpha_\sigma = 75^\circ$ differ by more than 1000% according to the data. The model can in fact capture such huge difference successfully as shown in Fig. 11b. The model also captures the concave upward shear-strain response of the data at this strain range, which is a product of the upward displacement of the DSL towards the unique CSL in the $e-p$ space, as the ζ tends towards zero with shearing (see Fig. 2b). If the effect of the fabric was not included in the model's formulation, the model would produce identical results for the tests of each series, with absolutely no differentiation of results according to the angle α_σ, i.e the exemplary difference of 1000% would not be possible to be simulated. Moreover, the model can also reproduce the softer and more contractive soil's response when b is increased, and this is observed if one compares tests and simulations for the same angle α_σ but different b value (in different Figures).

In Figs. 14–16, three series of tests (15 in total) with $b = 0.5$ as well as their corresponding simulations are presented. Each of the series has a different void ratio: $e = 0.86$ ($D_r \approx 30\%$), $e = 0.75$ ($D_r \approx 60\%$) and $e = 0.66$ ($D_r \approx 90\%$). The data are after (Nakata et al., 1998). In the plots the deviatoric stress is computed as $q_N = \left[0.5\left[(\sigma_1-\sigma_2)^2+(\sigma_2-\sigma_3)^2+(\sigma_3-\sigma_1)^2\right]\right]$ and the deviatoric strain as $\gamma_N = \left[2\left[(\varepsilon_1-\varepsilon_2)^2+(\varepsilon_2-\varepsilon_3)^2+(\varepsilon_3-\varepsilon_1)^2\right]/9\right]^{0.5}$. The data show that anisotropy has stronger effect in the $D_r = 30\%$ where for the large α_σ angles the soil is led to static liquefaction for deviatoric strains γ_N as low as 1-2%. For the densest soil

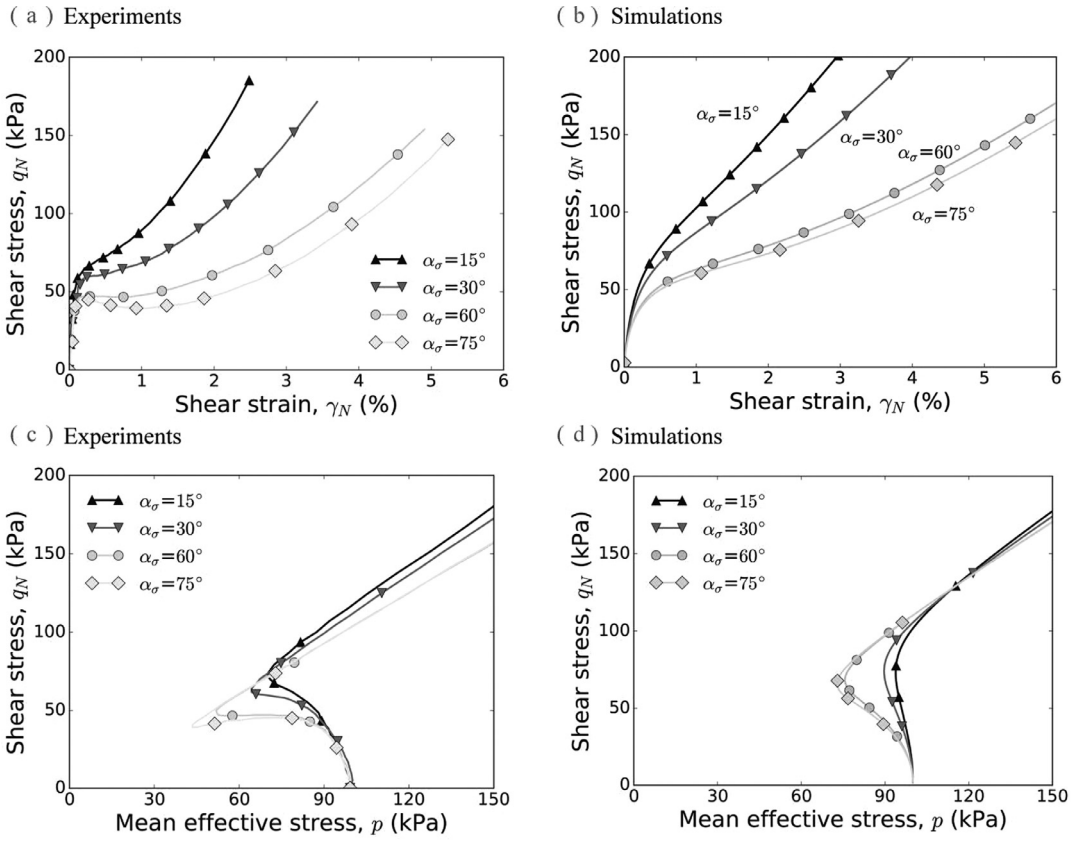

Fig. 15. Experimental data (a, c) and SANISAND-F simulations (b, d) for undrained shearing with constant $b = 0.5$ and constant $\alpha_\sigma = 15^\circ - 75^\circ$ on Toyoura sand with $D_r \approx 60\%$, $e = 0.754–0.768$. Data after Nakata et al. (1998).

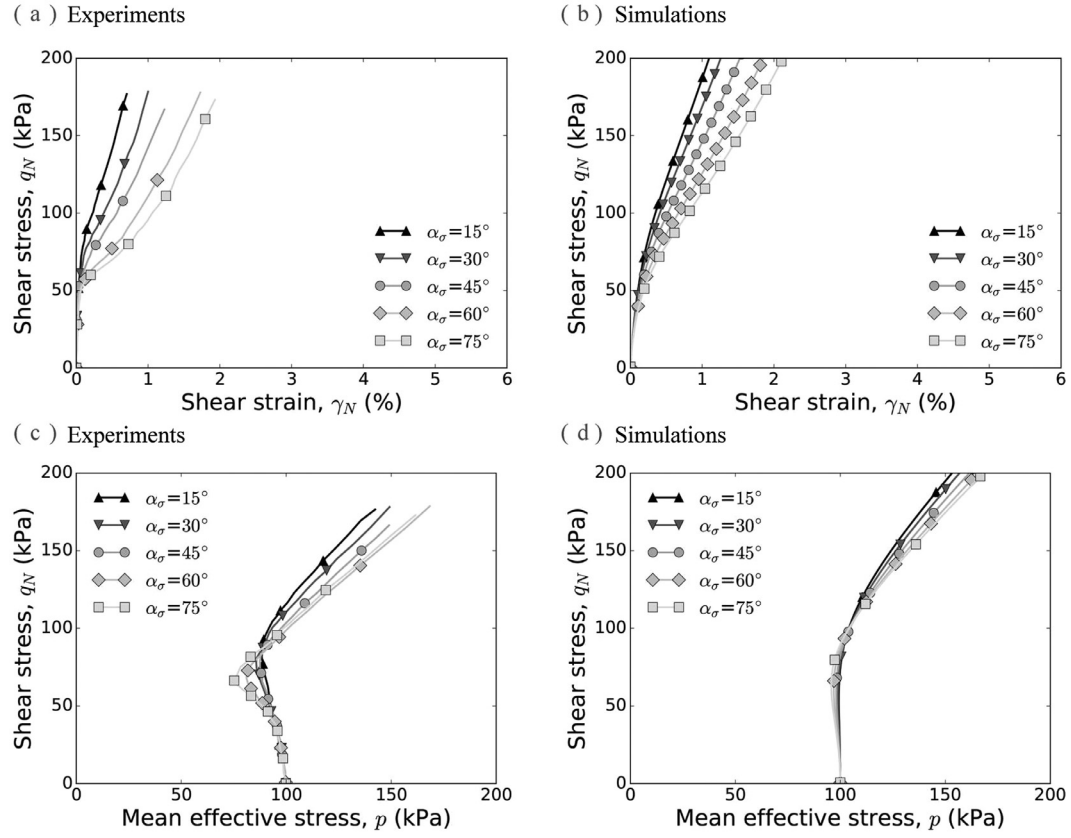

Fig. 16. Experimental data (a, c) and SANISAND-F simulations (b, d) for undrained shearing with constant $b = 0.5$ and constant $\alpha_\sigma = 15^\circ - 75^\circ$ on Toyoura sand with $D_r \approx 90\%$, $e = 0.652–0.659$. Data after Nakata et al. (1998).

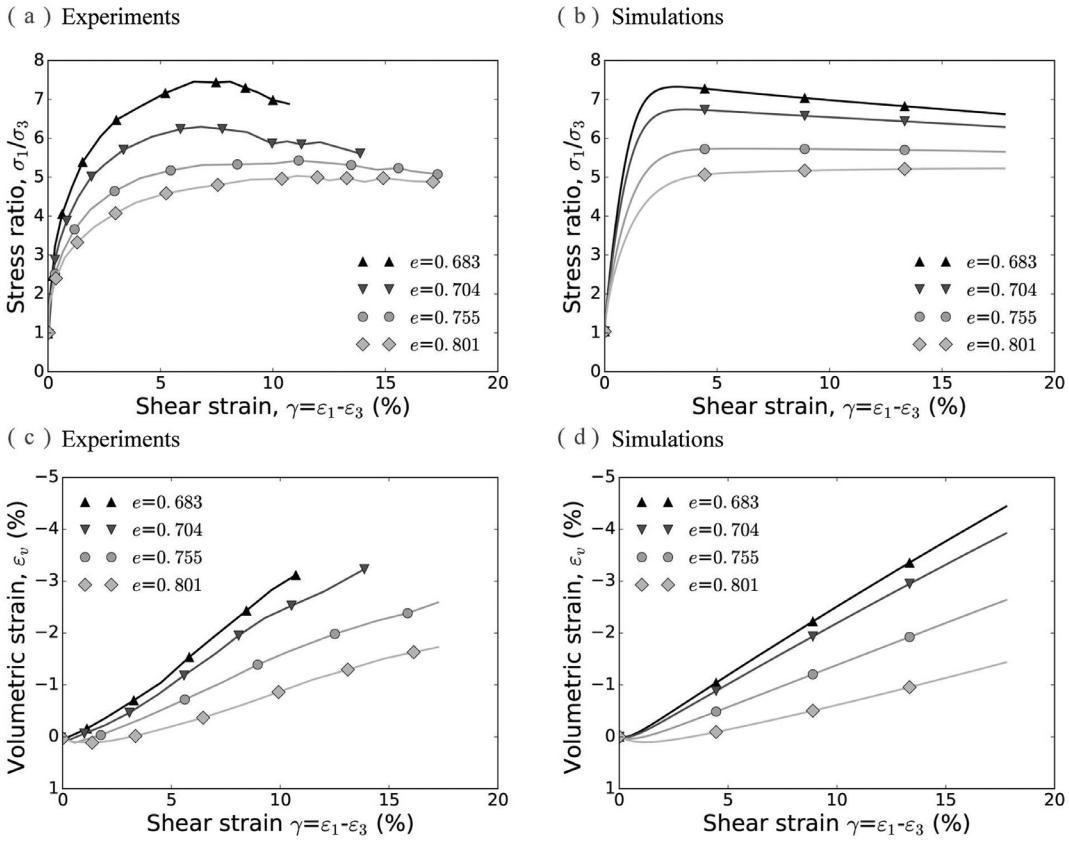

Fig. 17. Experimental data (a, c) and SANISAND-F simulations (b, d) for drained torsional shearing with constant $b = 0.5$, constant $\alpha_\sigma = 45^\circ$ on Toyoura sand with initial $p_0 = 50$ kPa and various void ratios. Data after Tatsuoka et al. (1986).

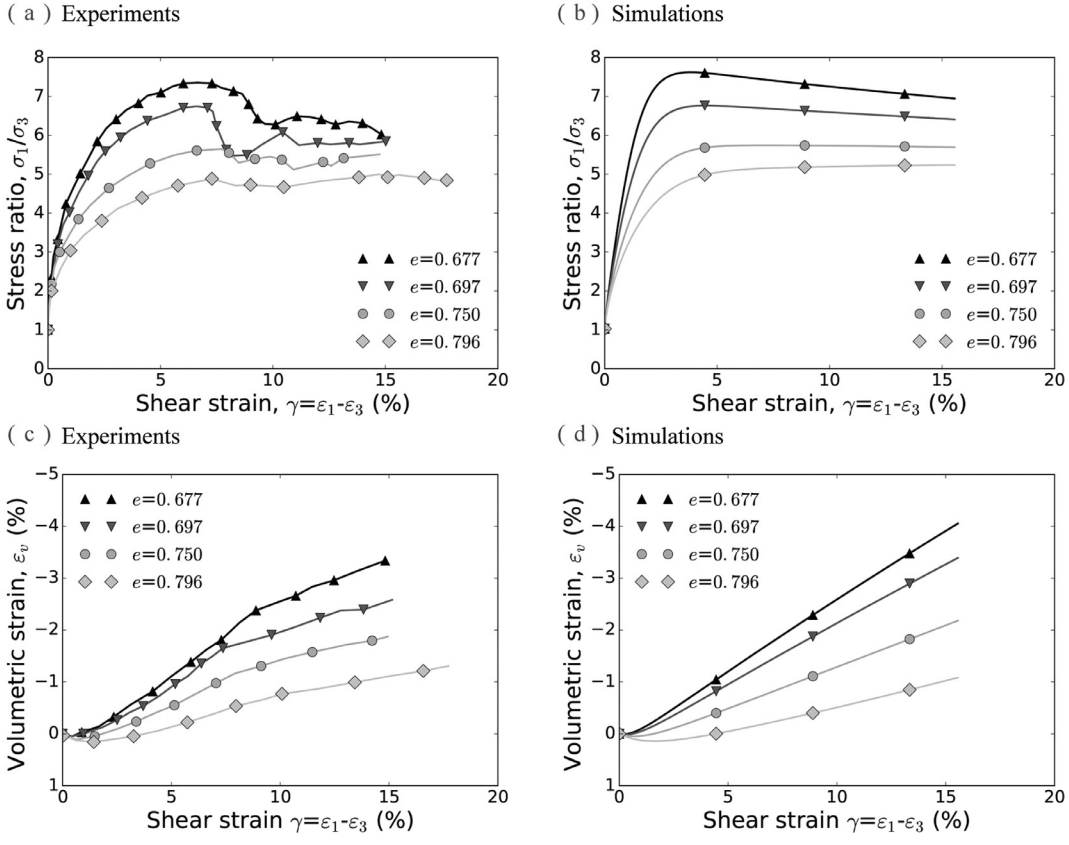

Fig. 18. Experimental data (a, c) and SANISAND-F simulations (b, d) for drained torsional shearing with constant $b = 0.5$, constant $\alpha_\sigma = 45^\circ$ on Toyoura sand with initial $p_0 = 100$ kPa and various void ratios. Data after Tatsuoka et al. (1986).

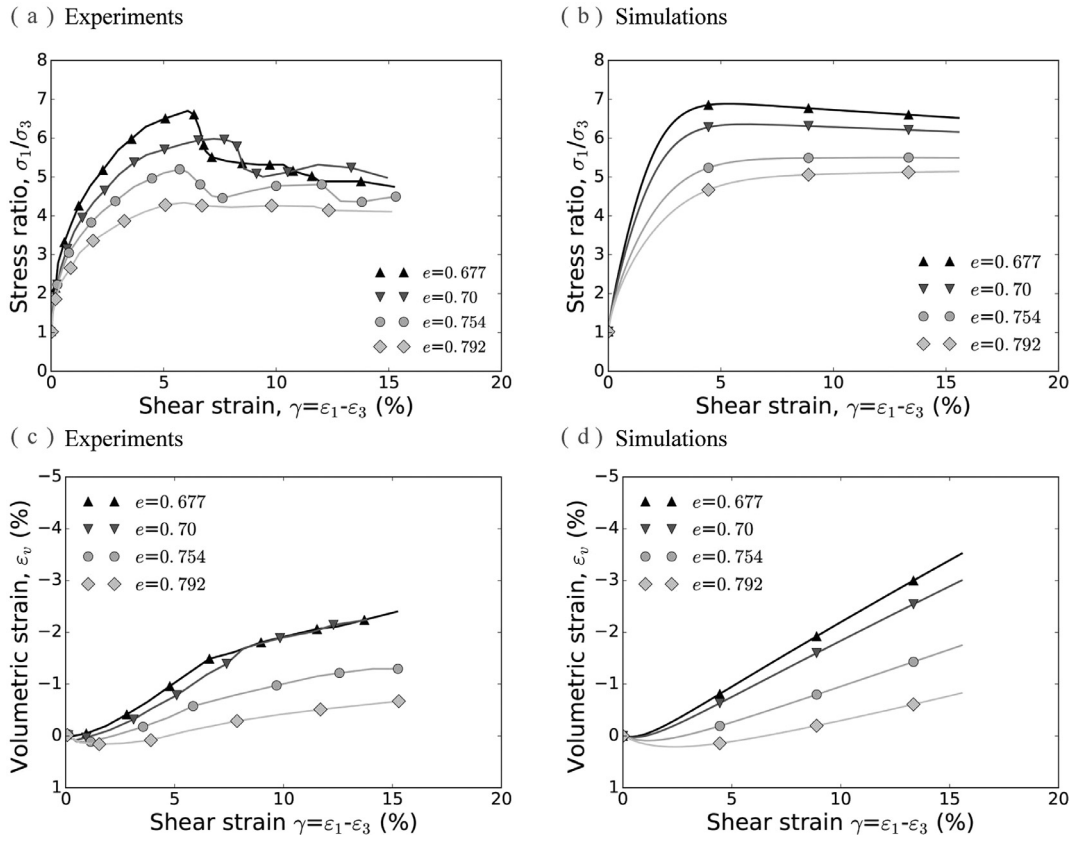

Fig. 19. Experimental data (a, c) and SANISAND-F simulations (b, d) for drained torsional shearing with constant $b = 0.5$, constant $\alpha_\sigma = 45^\circ$ on Toyoura sand with initial $p_0 = 200$ kPa and various void ratios. Data after Tatsuoka et al. (1986).

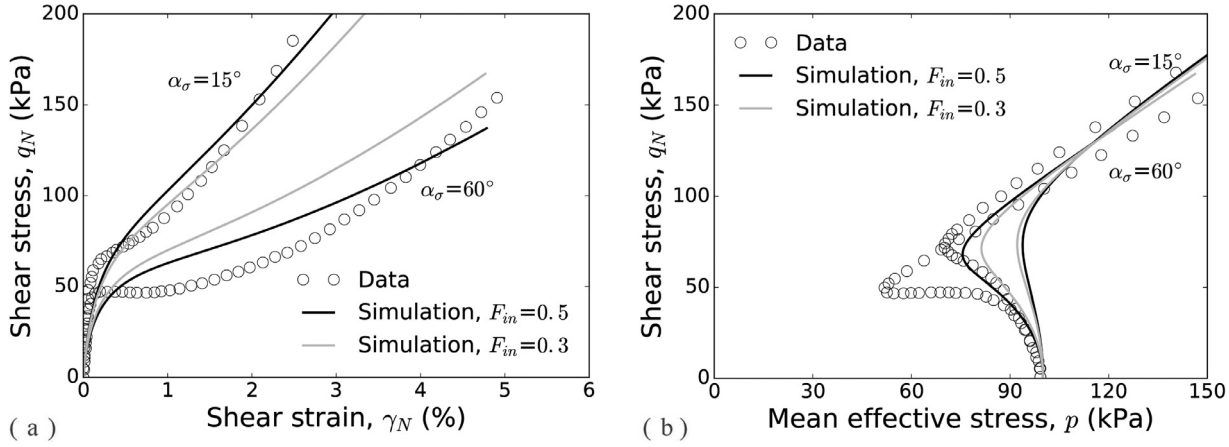

Fig. 20. Effect of initial fabric tensor norm (F_{in}) on model performance for undrained shearing with constant $b = 0.5$ and constant $\alpha_\sigma = 15^\circ$ and 60° on Toyoura sand with $e = 0.76$ ($D_r \approx 60\%$). SANISAND-F simulations against data after Nakata et al. (1998).

samples the effect of anisotropy is less pronounced, i.e. the difference in shear stress level for the same shear strain according to the angle α_σ becomes smaller with decreasing void ratio (increasing relative density). These trends are satisfactorily simulated by the model.

Note that Figs. 9–16 study the effect of angle α_σ on Toyoura sand response for different initial (p and e values) and loading (b value) conditions. The data and simulations show a widely different response, but ACST considers convergence to a common CS per triad of (p, e and b) regardless of the value of angle α_σ. The figures focus on model performance within the strain range of the available data and simply do not show this convergence that does appear only after very large shear strains (e.g. more than 50 %) as it will be discussed in the sequel in conjunction with Fig. 21.

Finally, drained torsional shear tests on Toyoura sand are also simulated, using the same set of model constants of Table 2. Figs. 17–19 present the experimental data and simulations for initial mean effective stress $p_0 = 50$, 100 and 200 kPa, respectively. For each of the three p_0 values, different initial void ratios are tested. During the tests, $b = 0.5$ and $\alpha_\sigma = 45^\circ$ are kept constant. The experimental data are after (Tatsuoka et al., 1986). The model reproduced the soil's response characteristics with good accuracy for these drained cases too. These successful simulations show that the state dependent dilatancy and plastic modulus formulations

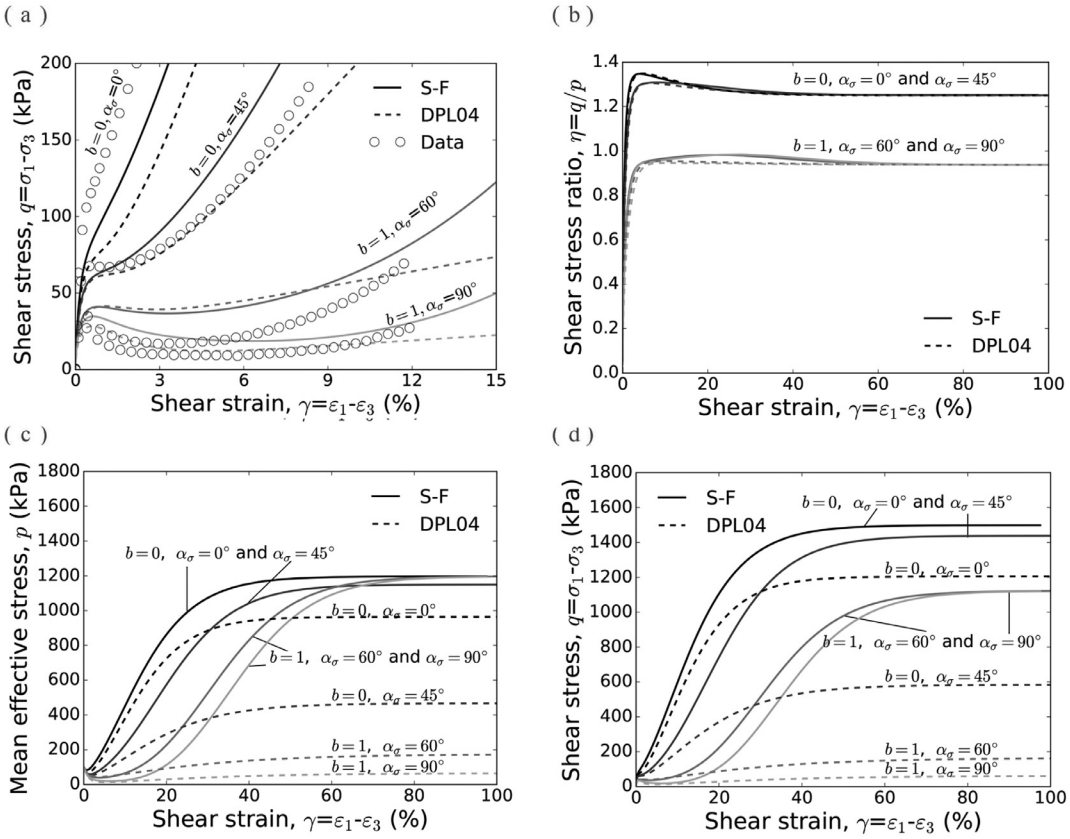

Fig. 21. Comparison between SANISAND-F (S-F; solid lines) with evolving fabric anisotropy and Dafalias et al. (2004) (DPL04; dashed lines) with inherent fabric anisotropy models in four different undrained tests with constant b and angle α_σ. The void ratio values are $e = 0.825$ in the test with $b = 0$, $\alpha_\sigma = 0°$; $e = 0.829$ in the test with $b = 0$, $\alpha_\sigma = 45°$; and $e = 0.826$ in both tests with $b = 1$, $\alpha_\sigma = 60°$ and $b = 1$, $\alpha_\sigma = 90°$. Data after Yoshimine et al. (1998).

can account for the effects of void ratio, confining pressure and fabric dependence.

4.3. Effect of initial fabric anisotropy

In all the numerical simulations presented above, a common value for the initial fabric norm $F_{in} = 0.5$ is used, corresponding to a transversely isotropic fabric. As explained in the calibration Section 4.1, the value for this model constant is hereby assigned and not measured. The assignment of a common value implies that all three employed datasets of Toyoura sand by Yoshimine et al. (1998), Nakata et al. (1998) and Tatsuoka et al. (1986) lead to the same initial fabric anisotropy, despite the use of different sample preparation methods and despite the small differences in maximum and minimum void ratios of the employed Toyoura sand batches in each publication. More specifically, Miura and Toki (1982) analyzed the characteristics of initial fabric of Toyoura sand samples and showed that pluviation methods, as used in Yoshimine et al. (1998) and Tatsuoka et al. (1986), induce the most anisotropic structures, while dry deposition used in Nakata et al. (1998) produces structures of intermediate anisotropy. Hence, the selection of a common F_{in} value is a simplifying assumption aiming to ascertain the simulative capabilities of the model even without fine-tuning the F_{in} value which could provide slightly better simulations.

However, it is interesting to investigate how sensitive are the simulation results for the data of Nakata et al. (1998), where the use of the dry deposition method is expected to lead to less initially anisotropic structures. For this purpose, two different tests from Nakata et al. (1998), presented in Fig. 15, with α_σ orientation at 15° and 60° respectively, are simulated again with a smaller $F_{in} = 0.3$, corresponding to a less initially anisotropic fabric. The results are presented in Fig. 20. The small $F_{in} = 0.3$ leads to a slightly more contractive response for the case when the orientation $\alpha_\sigma = 15°$ and to a less contractive response for the case where $\alpha_\sigma = 60°$. It is observed that the smaller $F_{in} = 0.3$ leads to a less anisotropic simulated response, since the two stress-strain curves of grey color tend to come closer to each other. It is concluded that the $F_{in} = 0.5$ is a reasonable value for these tests and the effect of a smaller Fin is small for low strain levels but higher for intermediate strain levels. However, the effect of the actual value of F_{in} is much less important than the initial fabric orientation with respect to the loading (measured via the angle α_σ herein). In addition, it must be remembered that the fabric tensor evolves towards its critical state value norm-wise and direction-wise, and consequently the difference in initial values fades away at large strains. In other words, our assumption for a same Fin for all three different preparation methods is judged as reasonable at least for the present case.

4.4. Evolving versus inherent fabric effects

The proposed model considers evolving fabric towards its critical state value that results into a unique Critical State Line (CSL) in the $e - p$ space within the ACST. Dafalias et al. (2004) have proposed a SANISAND type model that considers the effect of inherent and not evolving fabric, resulting into multiple CSLs in the $e - p$ space. In order to compare these two models' performance the following four undrained tests are simulated with both models: two tests with b=0, at $\alpha_\sigma = 0°$ and $\alpha_\sigma = 45°$ and two tests with $b = 1$, at $\alpha_\sigma = 60°$ and $\alpha_\sigma = 90°$, for which there are available experimental data for Toyoura sand by Yoshimine et al. (1998). The data and simulations are shown in Fig. 21, where the current SANISAND-F and the Dafalias et al. (2004) models are

abbreviated as S-F and DPL04 (initials of co-authors' names and publication year) models, respectively. The material constants of Table 2 are used for the S-F model, and those in Dafalias et al. (2004) for the DPL04 model. The void ratio values are e=0.825 in the test with $b = 0$, $\alpha_\sigma = 0^\circ$, $e = 0.829$ in the test with $b = 0$, $\alpha_\sigma = 45^\circ$ and $e = 0.826$ in both tests with $b = 1$, $\alpha_\sigma = 60^\circ$ and $b = 1$, $\alpha_\sigma = 90^\circ$.

As shown Fig. 21(a), both models simulate the up to 12% strain available experimental data with comparable accuracy, accounting successfully for the effect of stress principal axis orientation, with the S-F model showing a better simulation of the tendency to have a steeper stress-strain curve at strains greater than 12%. In the remainder subplots of this figure the strain range is increased to 100% and only the model simulations are compared among themselves. In Fig. 21(b), both models predict the same Lode angle dependent critical state stress ratio η_c with values M(b = 0) = 1.25 and M(b = 1) = 0.93 as expected, simply because the undrained stress path (not shown here) for both models converges very soon with the critical state stress ratios (but still is very far from critical state) at very different strain levels that cannot be shown in this figure. In Fig. 21(c) and (d), the S-F model predicts almost the same mean effective stress p_c and shear stress q_c at critical state, respectively, for all tests with the same Lode angle, as expected for a unique CSL in $e - p$ space inherent in ACST and in conformity with the basic feature of critical state theory (the small differences in p_c and q_c are due to small difference in void ratio values, namely $e = 0.829$ versus $e = 0.825$ and 0.826). On the contrary, the DPL04 model predicts largely different final p_c and q_c values for the same Lode angle at large strain, in violation of the basic feature of critical state theory, because the fixed fabric assumed in this model results into different CSLs depending on the relative orientation of fabric and principal stress axes.

These large differences in predicted response (at large strains) are of fundamental importance from a theoretical point of view (consider the thermodynamically consistent proof of uniqueness of the CSL presented in Li and Dafalias, 2012). For some practical applications, when the order of strain remains small, the (Dafalias et al., 2004) model (or alternatively the current model with fixed fabric tensor) can be a simpler alternative tool that does not require the calculation of an evolving fabric, but only the initial value of an inherent fabric tensor. However, there are several applications of high safety importance such as analyses of foundation failure, slope instability or active fault rupture propagation where shear strains reach very high levels leading the soil to critical state failure due to the formation of shearing zones, in which case the use of the evolving fabric related SANISAND-F is imperative for correct simulations.

5. Conclusions

The present model took the basic constitutive formulation of the (Dafalias and Manzari, 2004) bounding surface model that was compatible with classical critical state theory framework, and made it compatible with the new anisotropic critical state theory framework by Li and Dafalias (2012), where fabric effects became the new constitutive ingredients. The formulation is made within the SANISAND models platform that is based on bounding surface (BS) plasticity theory with kinematic hardening. The main goal of the model is to simulate the anisotropic response of sands due to fabric effects.

In ACST the fabric anisotropic variable (FAV) A is introduced as the trace of the product of the plastic strain rate and fabric tensor directions, acquiring the value 1 at critical state. In regards to constitutive modeling, A enters the definition of the dilatancy state parameter (DSP) ζ that substitutes for the classical isotropic state parameter ψ in the expressions of the dilatancy and plastic modulus. Mainly through ζ, but also through direct dependence of plastic modulus and fabric evolution rate on A, the effect of fabric anisotropy is transferred to the plastic strain rate components, enabling the SANISAND-F model to simulate accurately the anisotropic response of sands under drained and undrained shearing.

It is remarkable that by considering the effect of fabric anisotropy by means of A and ζ only in regards to dilatancy and plastic modulus, successful simulations of a wide range of undrained and drained torsional shear tests on Toyoura sand were achieved for various values of intermediate principal stress parameter b (ranging from 0 to 1) and orientation of major principal stress axis α_σ (ranging from 0° to 90°), Fig. 1. Difference in stress orientation can cause difference in the deviatoric stress at the same deviatoric strain level during undrained torsional shearing that can exceed 1000% in some cases (see Fig. 11); the model can capture such differences but notice that this would not be possible had fabric effects not been accounted for, in fact a single response would have been simulated for all loading orientations. This suggests the need to reconsider a wide range of constitutive models existing in the literature, including those of the SANISAND family, if such huge difference must be accounted for. Moreover, the model maintains the ability of previous SANISAND models without fabric effects to simulate the stress-strain relation and dilatancy response of sands for a very wide range of densities and confining pressures, under drained or undrained conditions using ζ instead of ψ in the dilatancy and plastic modulus definition. It is worth emphasizing that all these simulations were performed with a unique set of model constants and addressed data obtained at different times by three different laboratories for the same Toyoura sand. Last but not least, the model complies fully with the premises of Anisotropic Critical State Theory (Li and Dafalias, 2012) that encompasses those of the classical Critical State Theory (Roscoe et al., 1958; Schofield and Wroth, 1968).

It should be mentioned that reference to successful simulations might be contradicted by some deviations from experimental data, as it can be observed in Figs. 9–13, for example, when a sample is loaded at various orientations. But if one observes what is referred to in the previous paragraph for the simulations under a multitude of loading conditions (one can count 55 experiments simulated in this work) with a unique set of model constants, then the characterization of simulations as successful may be at least considered not an exaggeration. In passing notice that the simulations are performed with a linearized integration technique for incremental constitutive equations, proposed by Bardet and Choucair (1991) which by definition cannot consider the non-homogeneous stress and strain field that is possibly present in the tested samples (see Yoshimine et al., 1998 for a thorough discussion). Even though this can cause inaccuracies in the simulation of the material's stress-strain response, it is not expected to influence the presented comparisons significantly for two reasons: a) the combination of α_σ angles and b values of the simulated experiments are not prone to produce non-homogeneities (as discussed thoroughly in Yoshimine et al., 1998) and b) the strain levels that are analyzed remain relatively low (shear bands may be formed at larger strain levels when the stress state approaches the Critical State).

In conclusion, the new SANISAND-F model simulates successfully (within the aforementioned disclaimer on the meaning of "successfully") the vastly different anisotropic response of sands loaded at different orientations due to fabric effects, in addition to accounting for the effects of various relative densities, confining pressures and Lode angles (the intermediate principal stress effect via the value of b). Since the model is built within BS plasticity and uses kinematic hardening, it is able to qualitatively capture the main characteristics of cyclic loading response as other models of

the SANISAND family. However, more effort is needed for a quantitatively accurate cyclic response description that will be addressed in a future publication.

Acknowledgments

The research leading to these results has received funding from the European Research Council under the European Union's Seventh Framework Program (FP7/2007-2013) / ERC IDEAS Grant Agreement no 290963 (SOMEF) and partial support by NSF project CMMI-1162096 and the General Secretariat for Research and Technology of Greece (Matching Funds Program) under the project titled SOFI - SOil Fabric Investigation. Y.F. Dafalias acknowledges partial support by the European Regional Development Fund under Grant No. CZ.02.1.01/0.0/0.0/15003/0000493 (CeNDYNMAT). The authors would like to acknowledge and thank D. Papadopoulou for her help with the graphic design of the Figures. The authors would also like to thank the two anonymous reviewers for their help in enhancing the quality of the manuscript.

References

Andò, E., Viggiani, G., Hall, S.A., Desrues, J., 2013. Experimental micro-mechanics of granular media studied by X-ray tomography: recent results and challenges. Géotech. Lett. 3 (3), 142–146. doi:10.1680/geolett.13.00036.

Argyris, J.H., Faust, J., Szimmat, E.P., Warnke, E.P., Willam, K.J., 1974. Recent developments in the finite element analysis of prestressed concrete reactor vessels. Nucl. Eng. Design 28, 42–75.

Bardet, J.P., Choucair, W., 1991. A linearized integration technique for incremental constitutive equations. Int. J. Numer. Anal. Methods Geomech. 15, 1–19.

Been, K., Jefferies, M.G., 1985. A state parameter for sands. Géotechnique 35 (2), 99–112.

Chang, C.S., Hicher, P.Y., 2005. An elasto-plastic model for granular materials with microstructural consideration. Int. J. Solids Struct. 42 (14), 4258–4277. doi:10.1016/j.ijsolstr.2004.09.021.

Chaudhary, S.K., Kuwano, J., 2003. Anisotropic multiple yielding of dense Toyoura sand in p'-constant shear plane. Soils Found. 43 (4), 59–69.

Dafalias, Y.F., Manzari, M.T., 2004. Simple plasticity sand model accounting for fabric change effects. J. Eng. Mech. 130 (6), 622–634. doi:10.1061/(ASCE)0733-9399(2004)130:6(622).

Dafalias, Y.F., Papadimitriou, A.G., Li, X.S., 2004. Sand plasticity model accounting for inherent fabric anisotropy. J. Eng. Mech. 130 (11), 1319–1333. doi:10.1061/(ASCE)0733-9399(2004)130:11(1319) CE.

Dafalias, Y.F., Popov, E.P., 1975. A model of nonlinearly hardening materials for complex loading. Acta Mech. 21, 173–192.

Dafalias, Y.F., Popov, E.P., 1976. Plastic internal variables formalism of cyclic plasticity. J. Appl. Mech. 43, 641–646. doi:10.1016/0093-6413(76)90079-3.

Dafalias, Y.F., Taiebat, M., 2016. SANISAND-Z: zero elastic range sand plasticity model. Géotechnique 66 (12), 999–1013.

Duttine, A., Tatsuoka, F., Lee, J., Kongkitkul, W., 2009. Viscous property of Toyoura sand over a wide range of shear deformation rate and its model simulation. Soils Found. 49 (2), 231–247.

Fu, P., Dafalias, Y.F., 2011. Fabric evolution within shear bands of granular materials and its relation to critical state theory. Int. J. Numer. Anal. Methods Geomech. 35 (18), 1918–1948. doi:10.1002/nag.

Gao, Z., Zhao, J., 2015a. Constitutive modeling of anisotropic sand behavior in monotonic and cyclic loading. J. Eng. Mech. 141 (8), 04015017. doi:10.1061/(asce)em.1943-7889.0000907.

Gao, Z., Zhao, J., 2015b. Constitutive modeling of anisotropic sand behavior in monotonic and cyclic loading. J. Eng. Mech. 141 (8), 04015017. doi:10.1061/(ASCE)EM.1943-7889.0000907.

Gao, Z., Zhao, J., 2017a. A non-coaxial critical-state model for sand accounting for fabric anisotropy and fabric evolution. Int. J. Solids Struct. 106-107, 200–212. doi:10.1016/j.ijsolstr.2016.11.019.

Gao, Z., Zhao, J., 2017b. A non-coaxial critical-state model for sand accounting for fabric anisotropy and fabric evolution. Int. J. Solids Struct. 106-07, 200–212. doi:10.1016/j.ijsolstr.2016.11.019.

Gao, Z., Zhao, J., Li, X.-s., Dafalias, Y.F., 2014. A critical state sand plasticity model accounting for fabric evolution. Int. J. Numer. Anal. Methods Geomech. 38 (4), 370–390. doi:10.1002/nag.

Gutierrez, M., Ishihara, K., 2000. Non-coaxiality and energy dissipation in granular materials. Soils Found. 40 (2), 49–59. doi:10.3208/sandf.40.2_49.

Krieg, R.D., 1975. A practical two surface plasticity theory. J. Appl. Mech. 42 (3), 641. doi:10.1115/1.3423656.

Li, X., Li, X.-S., 2009. Micro-macro quantification of the internal structure of granular materials. J. Eng. Mech. 135 (7), 641–656. doi:10.1061/(ASCE)0733-9399(2009)135:7(641).

Li, X.S., 2002. A sand model with state-dependent dilatancy. Géotechnique 52 (3), 173–186.

Li, X.S., Dafalias, Y.F., 2002. Constitutive modeling of inherently anisotropic sand behavior. J. Geotech. Geoenviron. Eng. 128 (10), 868–880. doi:10.1061/(ASCE)1090-0241(2002)128:10(868).

Li, X.S., Dafalias, Y.F., 2012. Anisotropic critical state theory: role of fabric. J. Eng. Mech. 138 (3), 263–275. doi:10.1061/(ASCE)EM.1943-7889.0000324.

Li, X.S., Dafalias, Y.F., 2015. Dissipation consistent fabric tensor definition from DEM to continuum for granular media. J. Mech. Phys. Solids 78, 141–153.

Li, X.S., Wang, Y., 1998. Linear representation of steady-state line for sand. J. Geotech. Geoenviron. Eng. 124 (12), 1215–1217. doi:10.1061/(ASCE)1090-0241(1998)124:12(1215).

Loukidis, D., Salgado, R., 2009. Modeling sand response using two-surface plasticity. Comput. Geotech. 36 (1-2), 166–186. doi:10.1016/j.compgeo.2008.02.009.

Manzari, M.T., Dafalias, Y.F., 1997. A critical state two-surface plasticity model for sands. Géotechnique 47 (2), 255–272.

Miura, K., Miura, S., Toki, S., 1986. Deformation behavior of anisotropic dense sand under principal stress axes rotation. Soils Found. 26 (1), 36–52.

Miura, S., Toki, S., 1982. A sample preperation method and its effect on static and cyclic deformation-strength properties of sand. Soils Found. 22 (1), 61–77.

Mroz, Z., Norris, V.A., Zienkiewicz, O.C., 1979. Application of an anisotropic hardening model in the analysis of elasto-plastic deformation of soils. Géotechnique 29 (1), 1–34.

Mroz, Z., Zienkiewicz, O.C., 1984. Uniform formulation of constitutive equations for clays and sands. Mech. Eng. Mater. (April) 415–449.

Nakata, Y., Hyodo, M., Hidekazu, M., Noriyuki, Y., 1998. Flow deformation of sands subjected to principal stress rotation. Soils Found. 38 (2), 115–128.

Nicot, F., Darve, F., 2007. Micro-mechanical bases of some salient constitutive features of granular materials. Int. J. Solids Struct. 44 (22-23), 7420–7443. doi:10.1016/j.ijsolstr.2007.04.017.

Nicot, F., Darve, F., 2011. The H-microdirectional model: accounting for a mesoscopic scale. Mech. Mater. 43 (12), 918–929. doi:10.1016/j.mechmat.2011.07.006.

Papadimitriou, A.G., Chaloulos, Y.K., Dafalias, Y.F., 2018. A fabric-based sand plasticity model with reversal surfaces within anisotropic critical state theory. Acta Geotech. doi:10.1007/s11440-018-0751-5.

Papadimitriou, A.G., Dafalias, Y.F., Li, X.S., 2014. Anisotropic sand model and fabric evolution until the critical state. In: 8th European Conference on Numerical Methods in Geotechnical Engineering, Delft, pp. 85–89.

Petalas, A.L., Dafalias, Y.F., Papadimitriou, A.G., 2019. SANISAND-FN: an evolving fabric-based sand model accounting for stress principal axes rotation. Int. J. Numer. Anal. Methods Geomech. 43 (1), 97–123. doi:10.1002/nag.2855.

Richart, F.E., Hall, J.R., D., W.R., 1970. Vibration of Soils and Foundations. Prentice-Hall, Englewood Cliffs, NJ.

Roscoe, K.H., Schofield, A.N., Wroth, C.P., 1958. On the yielding of soils. Géotechnique 8 (1), 22–53.

Schofield, A., Wroth, P., 1968. Critical state soil mechanics. McGraw-Hill, London.

Sun, D., Huang, W., Yao, Y., 2008. An experimental study of failure and softening in sand under three-dimensional stress condition. Granul. Matter 10 (3), 187–195. doi:10.1007/s10035-008-0083-5.

Taiebat, M., Dafalias, Y.F., 2008. SANISAND: simple anisotropic sand plasticity model. Int. J. Numer. Anal. Methods Geomech. (32) 915–948. doi:10.1002/nag.

Tatsuoka, F., Sonoda, S., Hara, K., Fukushima, S., Pradhan, T.B.S., 1986. Failure and deformation of sand in torsional shear. Soils Found. 26 (4), 79–97.

Theocharis, A.I., Vairaktaris, E., Dafalias, Y.F., Papadimitriou, A.G., 2017. Proof of incompleteness of critical state theory in granular mechanics and its remedy. J. Eng. Mech. 143 (2), 04016117.

Theocharis, A.I., Vairaktaris, E., Dafalias, Y.F., Papadimitriou, A.G., 2019. Necessary and sufficient conditions for reaching and maintaining critical state. Int. J. Numer. Anal. Methods Geomech. (290963) 2041–2055. doi:10.1002/nag.2943.

Vaid, Y.P., Sivathayalan, S., 1996. Static and cyclic liquefaction potential of Fraser Delta sand in simple shear and triaxial tests. Can. Geotech. J. 33 (2), 281–289. doi:10.1139/t96-007.

Verdugo, R., Ishihara, K., 1996. The steady state of sandy soils. Soils Found. 36 (2), 81–91.

Wan, R., Nicot, F., Darve, F., 2010. Micromechanical formulation of stress dilatancy as a flow rule in plasticity of granular materials. J. Eng. Mech. 136 (5), 589–598. doi:10.1061/(ASCE)EM.1943-7889.0000105.

Wan, R.G., Guo, P.J., 2004. Stress dilatancy and fabric dependencies on sand behavior. J. Eng. Mech. 130 (6), 635–645.

Yang, Z.X., Wu, Y., 2016. Critical state for anisotropic granular materials: a discrete element perspective. Int. J. Geomech. 17 (2), 1–15. doi:10.1061/(ASCE)GM.1943-5622.0000720.

Yang, Z.X., Xu, T.T., Chen, Y.N., 2018. Unified modeling of the influence of consolidation conditions on monotonic soil response considering fabric evolution. J. Eng. Mech. 144 (8), 04018073. doi:10.1061/(asce)em.1943-7889.0001499.

Yoshimine, M., Ishihara, K., Vargas, W., 1998. Effect of principal stress direction and intermidiate principal stress on undrained shear behavior of sand. Soils Found. 38 (3), 179–188.

Zhao, J., Gao, Z., 2015. Unified anisotropic elastoplastic model for sand. J. Eng. Mech. 142 (1), 04015056. doi:10.1061/(asce)em.1943-7889.0000962.